Andean Geology 42 (2): 147-172. May, 2015
doi: 10.5027/andgeoV42n2-a01

Andean Geology
www.andeangeology.cl

Gravity derived depth to basement in Santiago Basin, Chile: implications for its geological evolution, hydrogeology, low enthalpy geothermal, soil characterization and geo-hazards

Gonzalo Yáñez[1, 2, 3], Mauricio Muñoz[2, 5], Valentina Flores-Aqueveque[2, 5], Andrés Bosch[4]

[1] *Departamento de Estructuras y Geotecnia, Pontificia Universidad Católica de Chile, Vicuña Mackenna 4860, Macul, Santiago, Chile. gyanez@ing.puc.cl*

[2] *Andean Geothermal Center of Excellence, Departamento de Geología, Universidad de Chile, Plaza Ercilla 803, Casilla 13518, Correo 21, Santiago, Chile. maumunozm@gmail.com, yokanti@gmail.com*

[3] *National Research Center for Integrated Natural Disaster Management, Edificio Hernán Briones, Tercer Piso, Vicuña Mackenna 4860, Macul, Santiago, Chile.*

[4] *Escuela de Ingeniería, Pontificia Universidad Católica de Chile, Vicuña Mackenna 4860, Macul, Santiago, Chile. andres.bosch.m@gmail.com*

[5] *Departamento de Geología, Universidad de Chile, Plaza Ercilla 803, Casilla 13518, Correo 21, Santiago, Chile.*

ABSTRACT. A recording of 1,115 gravimetric stations, the review of 368 wells, and the petrophysics measurements of 106 samples from representative outcrops have been used for a comprehensive geological/geophysical study of Santiago Basin. 2.5D and 3D gravimetric modeling, constrained by regional geology, soil and bedrock densities, edge-basin outcrops, depth (minimum) to basement from wells, and detailed modeling of heterogeneous bedrock and mid-crustal blocks, provided a well-constrained depth to basement model. Model results indicate the presence of a relatively shallow basin with an average of 250 m depth, and three sub basins with depth in excess of 500 m, but comprising less than 30% of the basin surface. From erosion rates in central Chile we estimate a basin infill lasting between 10 to 20 Ma. Basement topography/geomorphology, undercover a structural pattern dominated by NE and NW-trending structures that can be traced out of the basin, westwards in the Coastal Cordillera and eastwards in the Main Cordillera, with second order relevance of NS structures in the eastern border of the basin. This observation, further supported by natural crustal seismicity and basement-derived-magnetic signatures, suggests that the basin origin is mainly controlled by inherited old structures oblique to the margin. Active seismicity along these traverse NE and NW structures suggest that permanent deformation, and associated seismic hazard in the basin is mostly concentrated along these structures. The dynamic response of soils, in terms of the natural resonance frequency, shows that the basement-to-sedimentary/infilling-impedance-ratio is proportional to the amplitude of the resonance peak. On the other hand, the expected correlation between fundamental frequency and depth to basement is only partially supported by the empirical evidence. The difference between a greater gravimetric depth-to-basement compared to lesser seismic depth-to-basement, is attributed to changes in mechanical stiffness with depth compaction with minor effects in bulk density. Finally low enthalpy geothermal resources of the Santiago Basin is analyzed considering depth to bedrock, water table estimates and simple Darcy's-temperature coupled flow modeling. Results show that high groundwater temperature is restricted to deeper parts of southern sub-basin, which improves direct uses of geothermal energy for heating purposes.

Keywords: Gravity, Density, Sedimentary basin, Tectonics, Geo-hazards, Ground water, Low enthalpy geothermal resources.

RESUMEN. Profundidad del basamento derivado de la gravedad en la Cuenca de Santiago: implicancias para la evolución geológica, hidrogeológica, geotermia de baja entalpía, caracterización de suelos y peligros geológicos. El registro de 1.115 estaciones de gravedad, la revisión de 386 pozos, y la medición petrofísica de 106 muestras representativas de afloramientos se utilizaron para un estudio geológico/geofísico comprensivo de la Cuenca de Santiago. El modelamiento gravimétrico en 2.5D y 3D, constreñido por información geológica, densidad de suelo y roca, afloramientos del borde de la cuenca, profundidad de pozos (mínima) al basamento, y el modelamiento detallado de un basamento y corteza media heterogénea, ha permitido determinar una profundidad al basamento bien constreñida. Los resultados de la modelación indican la presencia de una Cuenca relativamente somera, con una profundidad media de 250 m, y tres subcuencas con espesores en exceso de 500 m, pero involucrando menos del 30% de la cuenca. A partir de las tasas de erosión en la zona central se estima un llenado de la cuenca de entre 10 y 20 Ma. La topografía/geomorfología de basamento revela un patrón estructural dominado por estructuras de orientación NE y NW, que pueden ser seguidas fuera de los límites de la cuenca al este y oeste, con estructuras NS de segundo orden en el borde oriental de la cuenca. Esta observación, sustentada además por sismicidad cortical y estructuras magnéticas de basamento sugiere que el origen de la cuenca está controlado por estructuras antiguas oblicuas al margen. La actividad sísmica a lo largo de estas estructuras transversales NE y NW sugiere que la deformación permanente y el riesgo sísmico asociado, está principalmente concentrado en estas estructuras. La respuesta dinámica de suelos, en términos de la frecuencia natural de resonancia, muestra que la razón de impedancia basamento/relleno es proporcional a la amplitud del 'peak' de resonancia. Por otra parte, la esperada correlación entre la frecuencia fundamental y la profundidad al basamento es solo parcialmente sostenida por la evidencia empírica. La diferencia entre una mayor profundidad al basamento gravimétrico comparado con una menor profundidad al basamento sísmico se atribuye a cambios en la rigidez mecánica producto de la mayor compactación, pero con cambios menores en términos de la densidad de los sedimentos. Finalmente, se analizan los recursos geotérmicos de baja entalpía en la Cuenca de Santiago considerando la profundidad al basamento, estimaciones de la profundidad a la napa freática, y modelos acoplados simples de flujo (Darcy)-temperatura. Los resultados muestran una alta temperatura del agua subterránea restringida a las partes profundas de las subcuencas del sector sur, la que mejora el uso directo de la geotermia con propósitos de calefacción.

Palabras clave: Gravedad, Densidad, Cuenca sedimentaria, Tectónica, Peligro geológico, Aguas subterráneas, Recursos geotermales de baja entalpía.

1. Introduction

Within the boundaries of Santiago basin there is the Chilean homonymous capital with more than 6.5 million inhabitants, constituting *ca.* 40% of the country population (INE, 2002). Together with high population density, the capital and surroundings concentrates a large amount of economic, political and social activities (INE, 2002). Therefore, an up-to-date geological knowledge of the territory, where the Santiago city is emplaced, is mandatory for its sustainable growth. Previous geological/geophysical studies in the basin have been focused on particular/isolated aspects, like hydrogeology (Falcón *et al.*, 1970; DGA, 2000), basin gravity-derived morphology (Kausel, 1959; Araneda , 2000), among others. In addition, most of these studies were accomplished several decades ago, lacking of considerable amount of local to regional data and new geological and geophysical knowledge acquired during the last decade. At this regard this research is focusing in a comprehensive geological/geophysical study of the basin, based on a compilation of surface geology and well logs, a new gravity database, the regional air-borne magnetic field, some local geo-electric surveys, and petro-physics of available outcrops. The geological well-logging for the wells located in the basin sedimentary infill and petro-physical properties of basement rocks constrained the interpretation of geophysical data (mostly gravity, but aided by the magnetic and geo-electrical fields) providing an estimate of the basin basement nature (morphology and degree of heterogeneity, Oligocene-Miocene volcano-clastic/intrusive) and infill (sedimentary cover within low-to-high energy fluvial/erosional domains), as well as potential structural domains that cross-cut and/or are bounding the basin. This basin characterization and solid geology estimate provide relevant implications for hydrogeology and geotechnical characterization of the basin (soil distribution, depth to basement and isolated sub-basins), low enthalpy geothermal assessment within the basin (heat transport by the groundwater flow pattern), and geo-hazards (major structural systems).

Here, we first describe the geological context in which Santiago basin is emplaced. In the second section we describe data gathered/compiled to achieve of the present study, which include surface geology, well description, measurements of physical properties

(magnetic susceptibility and density) of rock outcrops in the surroundings, gravity survey, and magnetic/geo-electrical compilations. In the interpretation chapter the full data set is integrated for a gravity-constrained modeling of 2D-3D solid geology. Finally we discuss hydrogeology, geotechnical, geothermal, and geo-hazards implications of this study.

2. Study area

Santiago basin (33°00'S-33°55'S and 70°30'W-71°0'W), is an irregular depression, located in central part of Chile (Fig. 1). This basin is part of the Central Depression, which is a north-south geomorphologic domain placed between Coastal Cordillera and Andean Cordillera (Fig. 1).

3. Geological Framework

Rock formations composing the basement of Santiago basin correspond to the eastern part of the Coastal Cordillera and the western part of the Andean Cordillera (Fig. 2). The first one is composed by Jurassic to upper Cretaceous volcanic and sedimentary sequences and Jurassic to Cretaceous intrusive rocks. The stratified formations conform a homoclinal fold, which dips 30-40° to the east (Gana *et al.*, 1996; Wall *et al.*, 1996; Wall *et al.*, 1999; Sellés and Gana, 2001).

Rocks from the western part of the Andean Cordillera correspond to continental, mostly volcanic and to a lesser extent sedimentary sequences, deposited during Cenozoic in Abanico intra-arc basin (Charrier *et al.*, 2002; Charrier *et al.*, 2005; Fock, 2005; Fock *et al*., 2006; Jara *et al.*, 2012; Jara and Charrier, 2014). This extensional basin was developed during successive tectonic events divided in two stages. First stage from Middle Eocene to Oligocene-Early Miocene was characterized by an extensional setting, which created depocenters, where Abanico Formation were accumulated (Charrier *et al.*, 2009). A second compressive stage linked to an increase in the plate convergence velocity-rate (Pardo-Casas and Molnar, 1987) dominated the evolution of the Abanico basin until Miocene. This change to a compressive regime, produced a partial tectonic inversion of the Abanico basin, from late Oligocene to early Miocene, inverting largest NS normal fault systems generated in the first stage (Godoy and Lara, 1994; Wyss *et al.*, 1994; Sellés, 1999; Charrier *et al.*, 2002; Charrier *et al.*, 2005; Fock, 2005; Fock *et al.*, 2006; Jara and Charrier, 2014). Folding and high angle fault reactivation was concentrated in basin edges during the second inversion stage (Fock *et al.*, 2006). The gradual crust thickening together with an intensive volcanic activity produced Farellones Formation deposition, in the central part of the basin and the emplacement of plutonic bodies, which intruded Cenozoic formations (Charrier *et al.*, 2002; Nyström *et al.*, 2003; Kay *et al.*, 2005; Muñoz *et al.*, 2006).

On bedrock, mainly gravel-to-sand size fluvio-alluvial and fluvial deposits have filled the basin, at least from lower Pleistocene, according to the dating of ancient alluvial fans (Rauld, 2011). Their origin is related to the fluvial systems conformed by Maipo and Mapocho rivers, which carry sediments from the Andean Cordillera westwards. Much less abundant, angular to sub-angular gravel in a medium-to-fine grain size matrix corresponding to colluvial deposits are located on the basin edges. Fine (silty sand to clay) lacustrine sediments can also be locally placed in the northwestern and southwestern of the basin. Pyroclastic deposits of the Ignimbrita de Pudahuel outcrops are mainly placed in the central western part of the basin. These deposits correspond to rhyolitic tuffs of Pleistocene age (Stern *et al.*, 1984), which in some cases are interstratified with fine alluvial sediments (Fig. 3).

4. Data compilation

Gravity information has been gathered during a long period of time (2006-2014), using different instruments (Gravimeters: Scintrex CG3 and Scintrex CG5 from IRD, Scintrex CG5 from Centro de Excelencia en Geotermia de Los Andes (CEGA); Differential GPS: ASHTECH SPECTRA-PRECISION, EPOCH 10, from Universidad de Chile (UCH), TRIMBLE C5 from Pontificia Universidad Católica (PUC)), despite the different equipments the standards have been kept in terms of accuracy (better than 0.1 mGal) and altitude errors (lower than 30 cm). With these constraints we estimate a gravity survey with a net error of 0.1 mGal. The gravity stations used in this study were 1,117, measured in four main surveys. A detailed specification of these surveys is presented in Table 1.

The GPS base stations of DGF and GEOCOM where linked in order to have a common datum

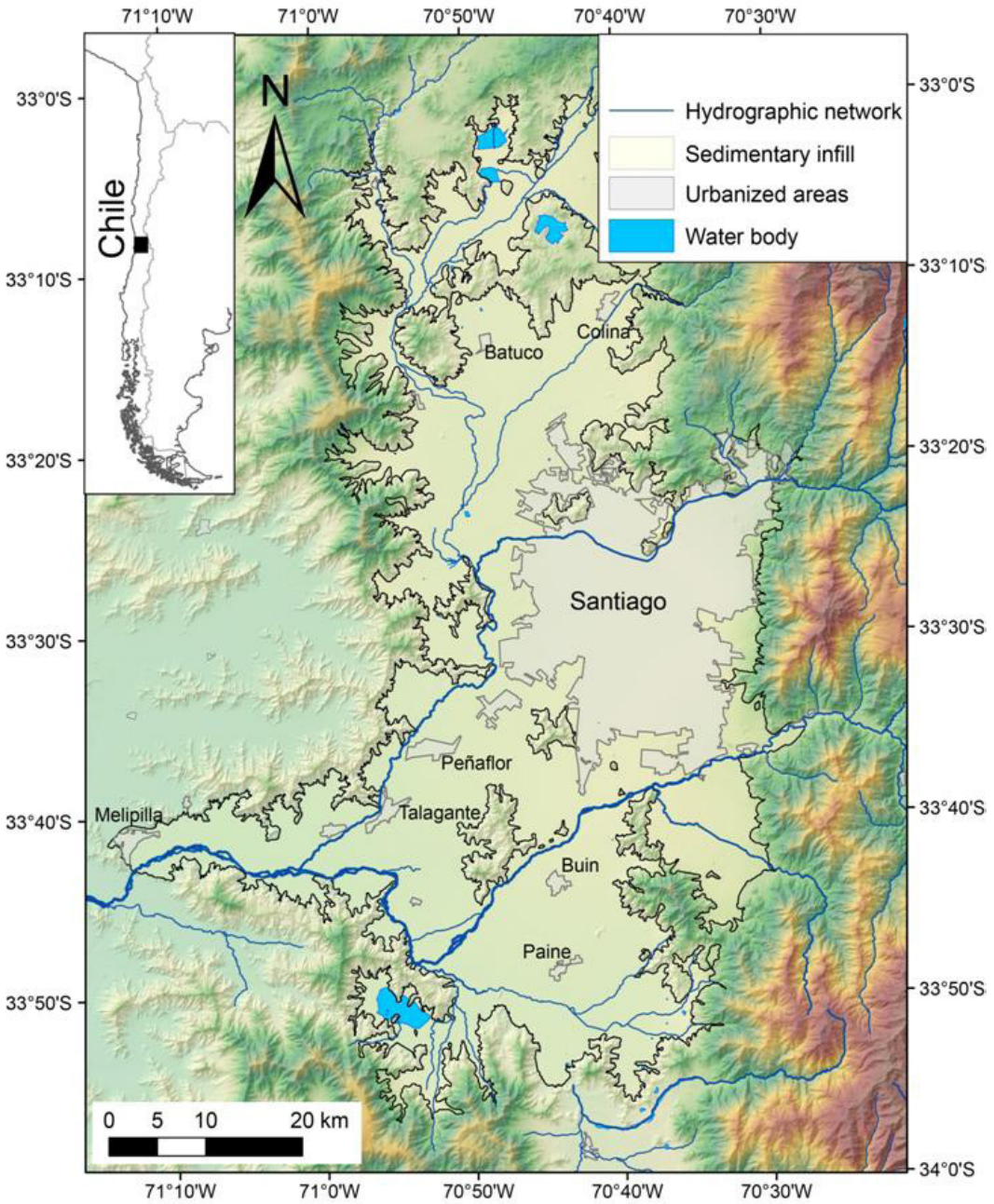

FIG. 1. Location of Santiago Basin.

for all the surveys. ANILLO, CEGA, and PUC, surveys where designed for regional purposes, considering an average station separation of 2-3 km, so they involved more than 90% of the study area and 621 stations. The remaining stations are restricted to the eastern border of the study area, belonging to a Master thesis in preparation. The purpose of this survey is rather different, a high resolution study of the basin border structures (San Ramón Fault). Nevertheless, we decided to include

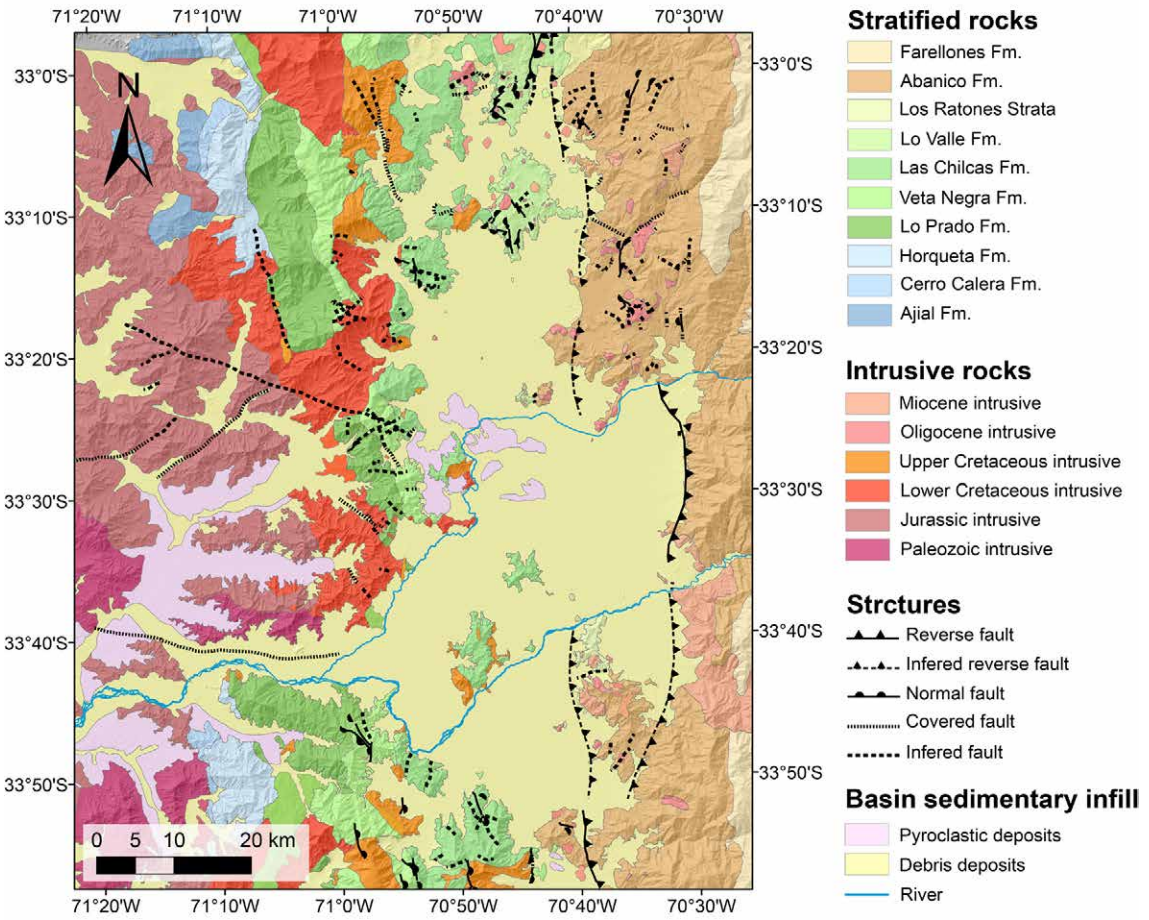

FIG. 2. Geological map of basement rocks of Santiago Basin (Modified of Gana *et al*., 1996; Wall *et al*., 1996, 1999; Sellés and Gana, 2001; Fock, 2005 and Fuentes *et al*., 2002).

this data in the whole basin compilation, because it provides a good resolution for a relevant domain of the Santiago Basin. In summary we complete this gravity study over 3,000 km^2, with one station every 5 km^2. In figure 4 we show the data distribution over the basin and associated borders. As shown in the figure 4, survey design considers most of the measurements over the sedimentary cover, however we care of taking at least 5% of the data over basement outcrops to insure a good estimate of the regional gravity field.

Data acquisition and reduction consider the standard procedure for gravimetric surveys (*e.g.,* Telford and Sheriff, 1990). Gravity data were acquired using loops against a base station. The gravimetric instruments used in the survey compute continuously the tidal variation, so a linear instrument drift during the day is good enough resolved with measurements in the base station at the beginning and end of each survey day. The latitude corrections, due to the earth shape and rotation were computed using the WGS84 reference ellipsoid. The absolute gravity value was obtained using the base station at the Departamento de Geofísica of Universidad de Chile (Gravity DGF: 979416.07 [mGal]). Differential GPS provides an altitude above the sea level (WGS84 datum) for Free Air and Bouguer Correction (Telford and Sheriff, 1990). To perform the Bouguer Correction we assumed a density of 2.67 [gr/cc]. Even though this is a rather arbitrary assumption, the basement heterogeneity makes useless a more refined treatment of this parameter. This variability will be taken into account later on in the modeling effort for the regional field estimate. Terrain cor-

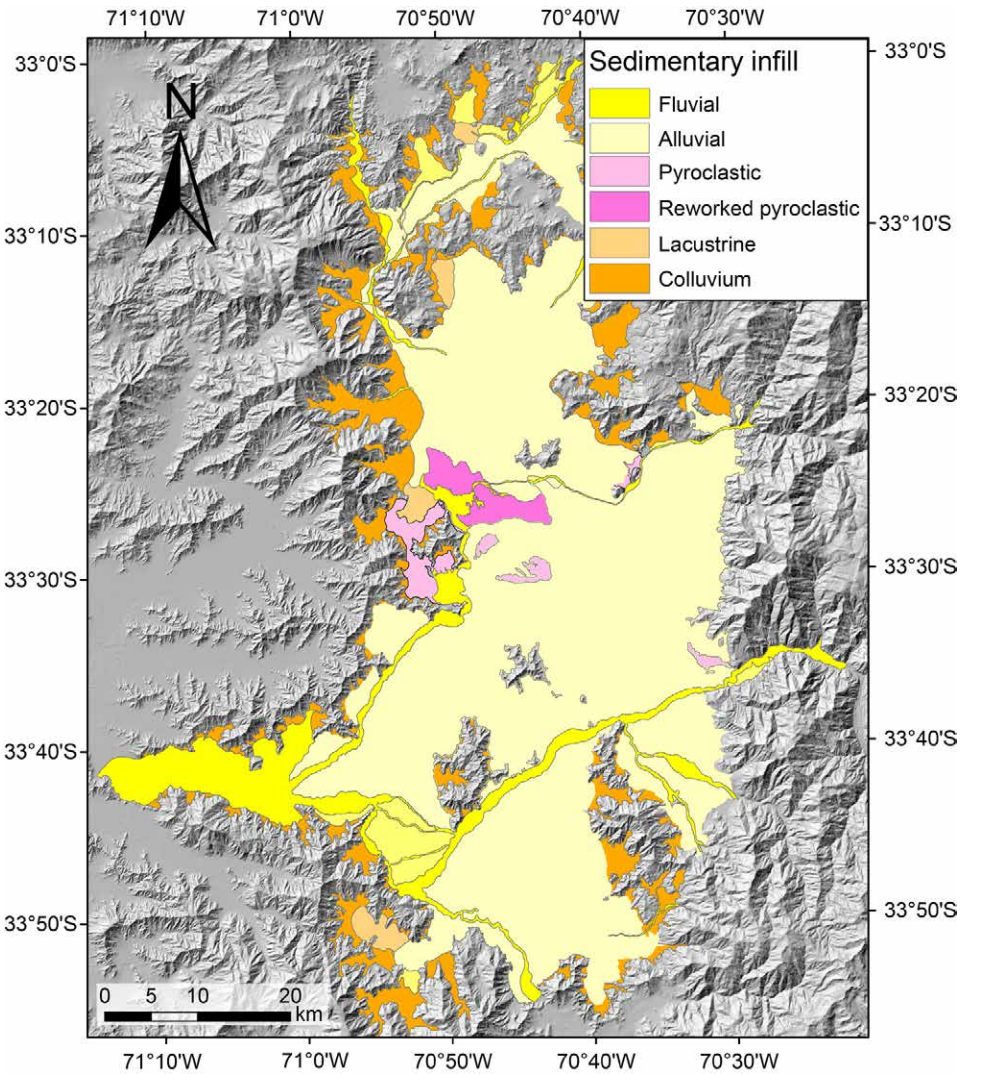

FIG. 3. Superficial distribution of the sedimentary infilll in Santiago basin (Modified of Brantt, 2011; Gálvez, 2012 and Rauld, 2011).

rection also considers a mean density of 2.67 [gr/cc], over a digital terrain model (DTM) of 30 m resolution. The relief in the study area has slopes below 30°, therefore resolution of the DTM model is good enough to insure that Terrain Correction is not underestimating the topographic effect. The Bouguer Anomaly obtained after the application of all this corrections is shown in figure 4, a hillshade of the digital terrain model was used in this figure as a base frame. The pattern of this anomaly is the expected response in the Central Andes (Dragicevic, 1970), with a negative gradient towards the East, as a result of the cuasi-isostatically equilibrated crustal roots of the High Andes (*e.g.,* Tassara and Yáñez, 2003). According to figure 4, regional gradient ranges from -3.14 [mGal/km] in the northern flank of the study area, to -2 [mGal/km]. As we will see later on, this variability is mostly due to mid crustal heterogeneities. The Bouguer Anomaly described in figure 4 is the basic gravity information used in the remaining part of this study, its modeling and interpretation requires a precise knowledge of the density properties of rocks and soils present in the study area and underneath. In the next section we describe the petrophysics of the exposed rocks and sediments, including well logging data.

TABLE 1. GRAVITY SURVEYS INCLUDED IN THIS STUDY.

Survey	Gravimeter	GPS	GPS Base	Survey date	N# stations
ANILLO Project	Scintrex CG3 (IRD)	ASHTECH-S-PRECISION, EPOCH 10 (UCH)	DGF	2006-2008	100
CEGA	Scintrex CG5 (CEGA)	TRIMBLE C5 (PUC)	GEOCOM	2012-213	254
PUC	Scintrex CG5 (CEGA	TRIMBLE C5 (PUC)	GEOCOM	2012-214	265
PUC-FSR	Scintrex CG5 (CEGA	TRIMBLE C5 (PUC)	GEOCOM	2012-214	496
DGPS BASE: • DGF (33.4573°S, 70.6620°W • GEOCOM (33.4437°S, 70.6238°W)				TOTAL: 1,115	

5. Petrophysics/Well Logs

Basement rocks are found, mostly, in the flanks of the basin. We collected 106 rock samples from outcrops, trying to get an appropriate representation of all the geological units present in the study area. In figure 4 we show the location of the outcrop samples for petrophysical analysis (density/ magnetic susceptibility). Magnetic susceptibility was measured with the KT-10 Susceptibility meter. Density measurements were obtained through the ratio of rock weight at air (Wair) and water-immerse (W_{water_i}):

$$[\rho = \frac{w_{air}}{w_{air} - w_{water\_i}}]$$

The instrument error is 10 gr per 1 kg, hence for 1-2 kg samples, the density errors range between 1-2%, equivalent to 0.02-0.04 gr/cc. In figure 5 we show the average values for the main unit/formation of the study area in terms of density and magnetic susceptibility values. Larger density values are observed for intrusive units, in particular the Cretaceous sequence, in agreement with the larger values of magnetic susceptibility. This correlation implies the relevance of the mafic composition on these units. Volcano-sedimentary units show a slightly lower density, in particular Lo Valle formation. In this case the low density is due to the mix of sedimentary (less dense, non-magnetic), and igneous components (dense as intrusive source of similar composition, and magnetic).

The density estimation for the Santiago basin sedimentary infill, was prepared based on stratigraphic descriptions of 991 boreholes from four data sources: **1.** 67 borehole descriptions were provided by the Centre of Research, Development and Innovation of Structures and Materials (IDIEM, Universidad de Chile); **2.** 56 wells reports were compiled from APR (Rural Drinking Water Services); **3.** 500 borehole descriptions were provided by Milenio Project (Seismotectonics and Seismic Hazard, Universidad de Chile), and **4.** the stratigraphic information of 368 wells were collected in field and from the Dirección General de Aguas (DGA) expedients.

The estimation of the density for the sedimentary infill was done by assigning density values to each type of sediments, based on typical density values (*e.g.,* Linsley *et al.*, 1982; Poffijn *et al.*, 1988) and from estimate of the relative content of gravel, sand and silt/clay. The density values range between 1.72 and 2.08 g cm^{-3} for the end members clay and gravel, respectively. For pyroclastic deposits a value of 1.71 g cm^{-3} was used (Mues-Schumacher *et al.*, 2004). With these values, the mean density of each borehole was calculated by weighted average by the thickness of each layer. A surface which represents the density was determined by interpolating each control points with ordinary Kriging, using a circular model without anisotropy (Fig. 6).

The higher density estimations are mainly concentrated in a NE fringe located in the south-central part of the basin, coinciding with the Maipo river alluvial fan, which deposited coarser sediments within the basin. The northern part and southern end of the basin contain lesser density sediments, because these alluvial fans were deposited in a

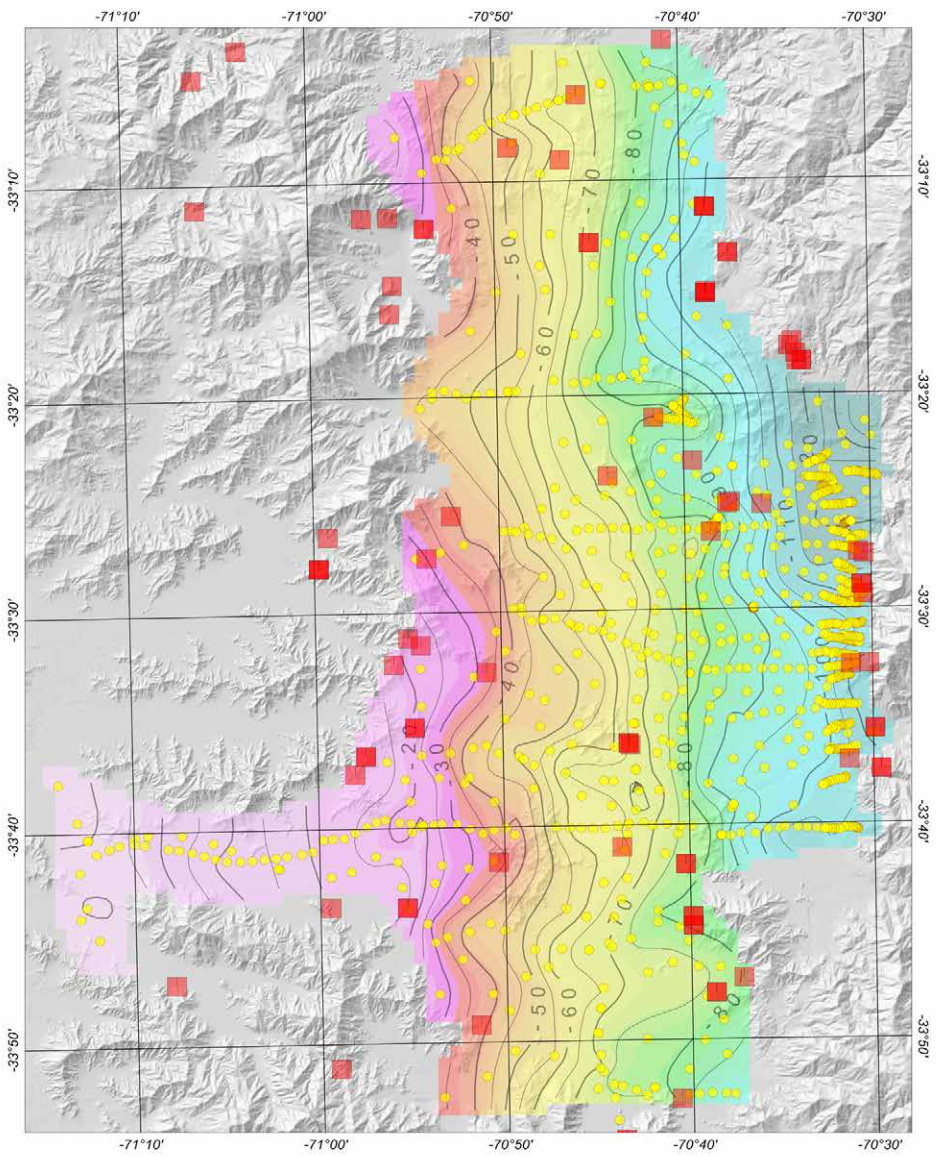

FIG. 4. Bouguer anomaly (colours) over hillshade (gray shaded). In addition we include the location of the gravity stations (yellow circles) and the petrophysics sampling location (red squares).

lower energy environment. Particular sectors with low-density sediments are related to lacustrine or pyroclastic deposits.

6. Regional estimate and 2D-3D basin modeling

Basin modeling requires a precise estimate of the regional field. In a complex basement/crustal structure the standard procedure (*e.g.,* Telford and Sheriff, 1990) is not accurate enough, so we adopt a sequential approach described in the following paragraph and represented graphically in figure 7. Bouguer Anomaly (Fig. 4) shows the typical eastward negative trend associated with the crustal-root-low-density domain. We remove this long wavelength trend computing the gravimetric response of the 3D, continental scale, density model of South America (Tassara *et al.*, 2006) (Fig. 7a, Regional-1). Figure 7b represents the gravity field after the removal of the continental-scale field (Residual-1). Looking at

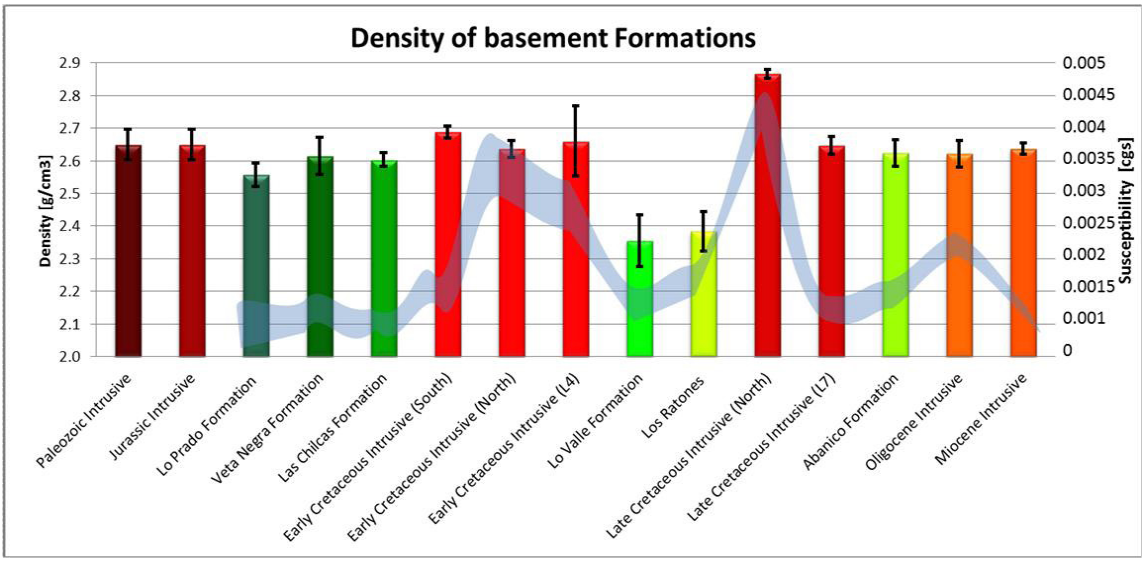

FIG. 5. Density/magnetic susceptibility average for the main units/formations of the study area. Magnetic susceptibility is shown in light blue, the thickness of the ribbon represents the statistical variability.

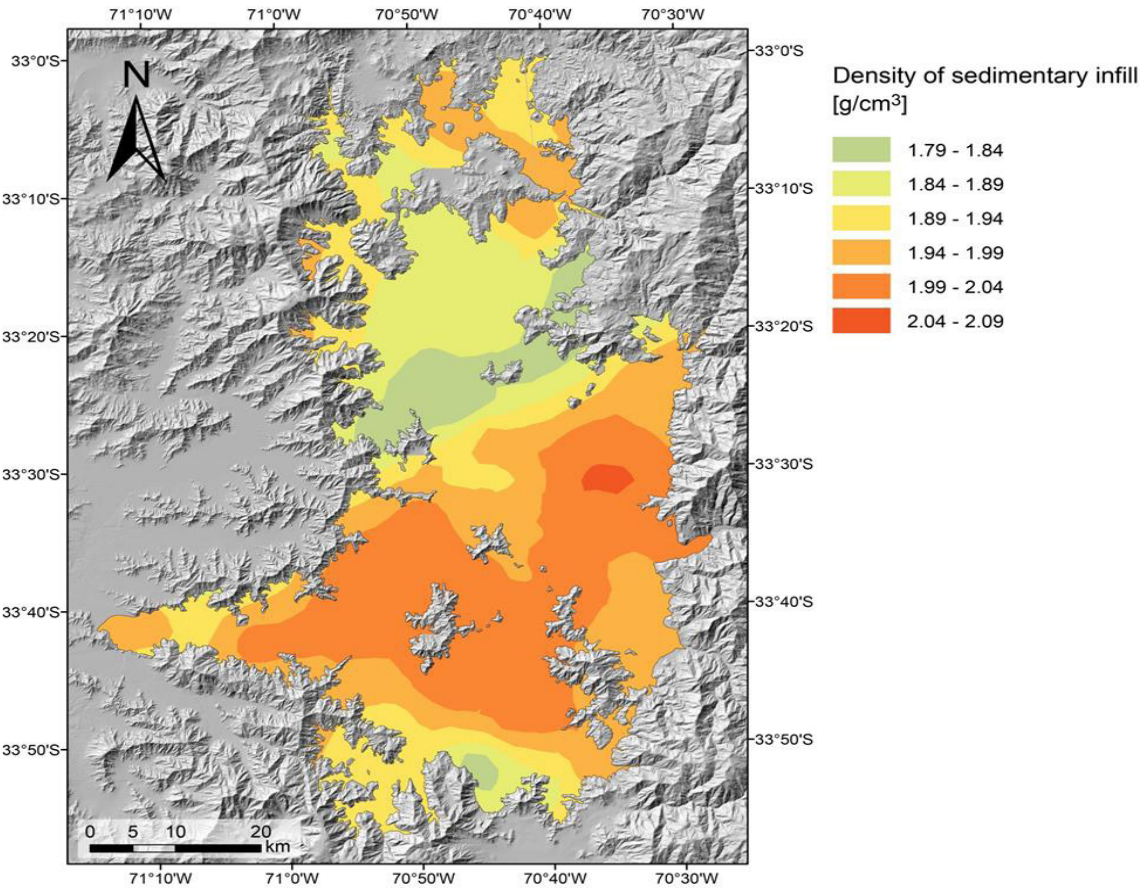

FIG. 6. Density of the Santiago basin sedimentary infill.

this gravimetric field we see that this field does not resemble the typical response of a basin with a low density infill (mostly negative signals). In fact, the east and mostly the south east zone show a large positive anomaly of tens kilometer wavelength. From previous studies (Yáñez *et al.*, 2008; Yáñez and Rivera, 2009; Rivera and Cerda, 2012), this positive anomaly is interpreted in terms of a dense mid-crustal body. In order to remove this effect we formally model the effect of a mid-crustal dense body. To perform this computation we require a constraint for the depth to the source and the density contrast. Depth to the source is estimated through the slope of the power spectrum of Residual-1, according to the scheme developed by Spector and Grant (1970). In figure 8 the slope of the power spectrum show a maximum depth of 8 km, this depth is interpreted as the roof of the dense body. The shape and density of the dense body is obtained by trial and error 3D forward modeling using ModelVision package. A density of 3 [gr/cc] fit the gross amplitude of Residual-1. Figure 7c represents the model response of the dense mid-crustal body located at a depth of 8 km (Regional-2). The residual obtained after its removal, Residual-2, is presented in figure 7d. This Residual-2 field contains the effect of the basin infill and the heterogeneous basement. In order to remove the effect of the heterogeneous basement, we perform a series of 2.5D forward models along 10 EW transects (see locations in figure 7f). These forward models effort are constrained by the available well logs in the study area, the density constraint provided by the basement outcrops (Fig. 5), the sediment density estimates (Fig. 6), and a reference density of 2.67 [gr/cc]. An example of this modeling is presented in figure 9, the whole models are described in detail in Bosch (2014). With the 2.5D response of the 10 profiles we compute the isolated effect of the sediment infill. This sediment-infill response is gridded and subtracted to the Residual-2 field. The smoothed response of this operation represents the last regional applied to the observed data (Fig. 7e). This Regional-3 accounts for the heterogeneous basement density distribution of the study area. Finally Residual-3 (Fig. 7f), which represents the difference between Residual-2 and Regional-3, is the gravity field used for 3D modeling of the basin infill.

Residual-3 is used to perform a 3D inversion model. The effect of mid-crustal bodies and basement heterogeneity have been removed already, therefore we only need to model the depth to basement of the sedimentary infill. Density infill values are taken from figure 6. This density field is considered the representative value for each discrete prism of 500x500 m horizontal section. Gravimetric modeling is calculated using the prismatic algorithm described by (Plouff, 1976). 3D gravimetric inversion is implemented in Matlab according to the following scheme:

1. Estimate of first prismatic thickness $(h_{i,j}^{o})$ using the slab formula:

$$h_{i,j}^{o} = \frac{g_{i,j}}{2\pi G(\rho_{i,j} - \rho_{ref})}$$

2. Computation of model response using the prism model: $g_{i,j}^{M}$

3. Determine the increment (reduction) of k-th iteration of the prismatic thickness $(h_{i,j}^{k})$, according to the following formula:

$$h_{i,j}^{k} = h_{i,j}^{o} + \frac{g_{i,j} - g_{i,j}^{M}}{2\pi G(\rho_{i,j} - \rho_{ref})}$$

4. Compute the model response considering the new depth to basement, and determine the misfit between the model response and the observations. If the obtained misfit is larger than the expected value return to step 2), in the contrary stop the process.

Model inversion result is presented in figure 10 (left panel) in companion with the obtained misfit, which is stable after the 4th iteration with a value below 0.05 [mGal], that represents less than 1% of the observed signal (between 5-10 [mGal]). Border depths to basement must be taken with caution, because 3D inversion performance at these cases is hampered by the size of the grid (1,000 m) and the lack of a full data control (in some areas data interval is even more than 2 km). In the right panel of figure 10 we include the topography relief after removing the sedimentary cover, by subtracting the depth to basement from the digital terrain model. The goodness of this 3D modeling effort is tested against the depth to basement observed in wells. This comparison is presented in figure 11 (left panel). Notice that most of the well depths are in fact minimum depths because they didn't reach the basement. We do see that model response for shallow depth to basement show a good agreement with the observed depth in wells. On the other hand, for deeper depths to basement the model response are generally larger than well depth. This is a reasonable result because deeper wells generally do not reach the basement. In

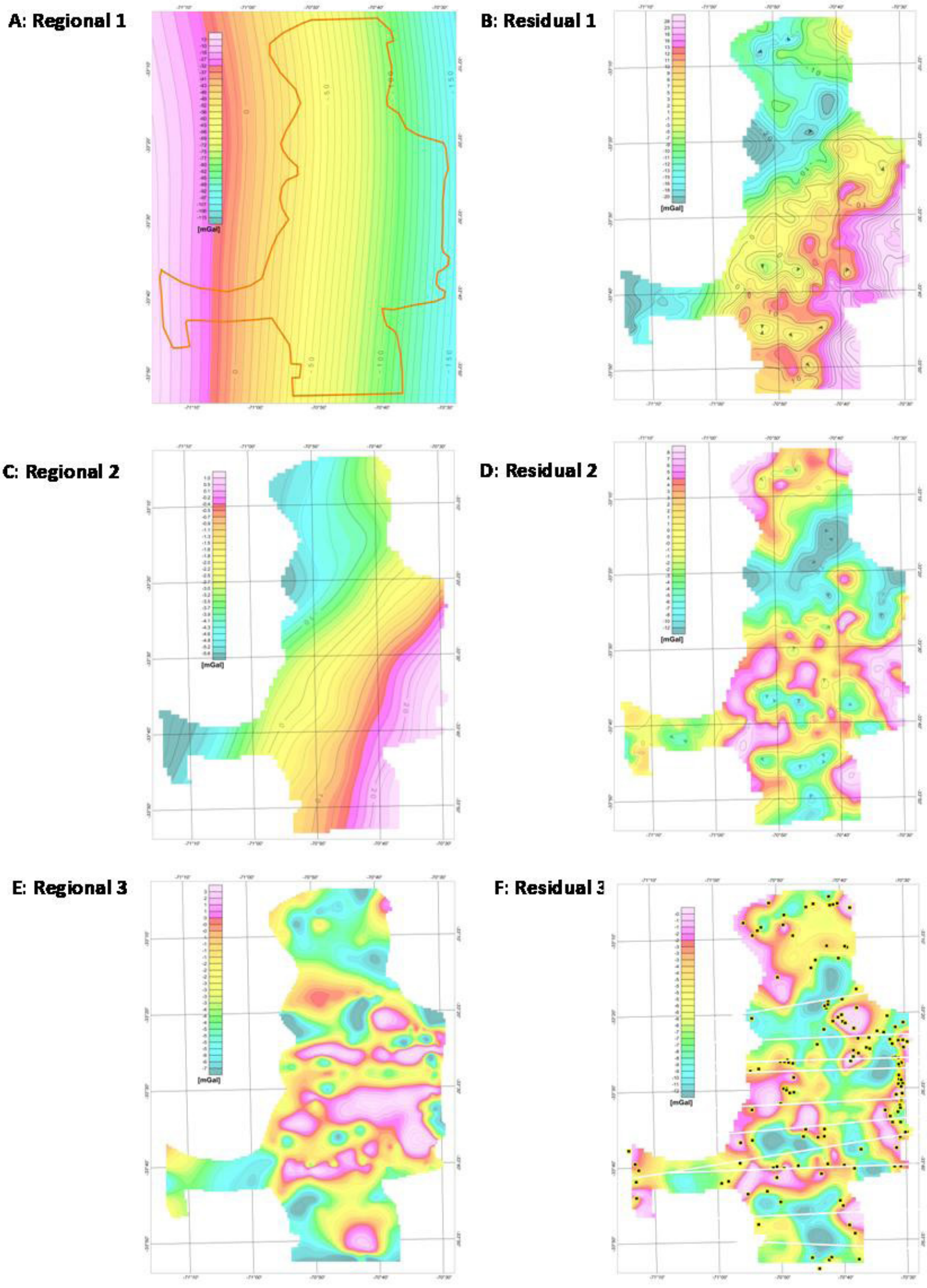

FIG. 7. Regional estimation map sequence. In figure F the Residual-3 field is superimposed to the 2D forward modeling (white lines) and outcrops control points (black dots).

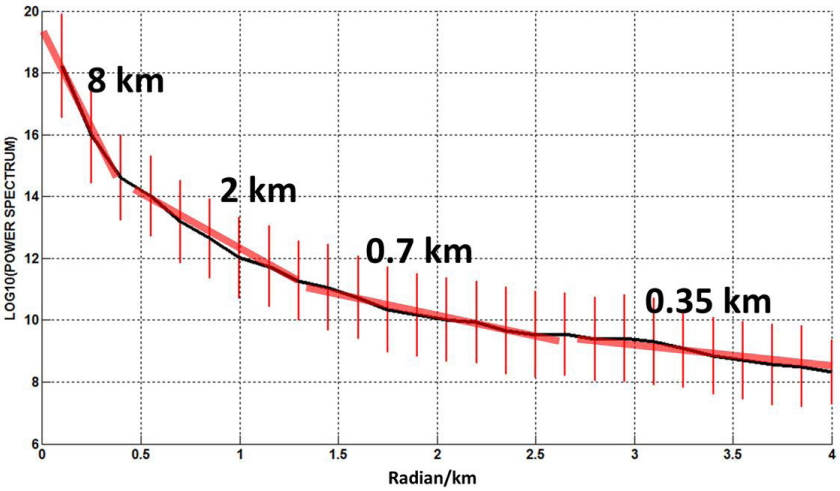

FIG. 8. Power spectrum of gravity field: Residual 1 (Fig. 7c). The 8 km slope of the largest wavelength represents the roof of the deepest source, for shorter wavelengths the spectrum indicates the depth to shallower gravimetric sources. Vertical red lines are the error bars of each spectrum estimate.

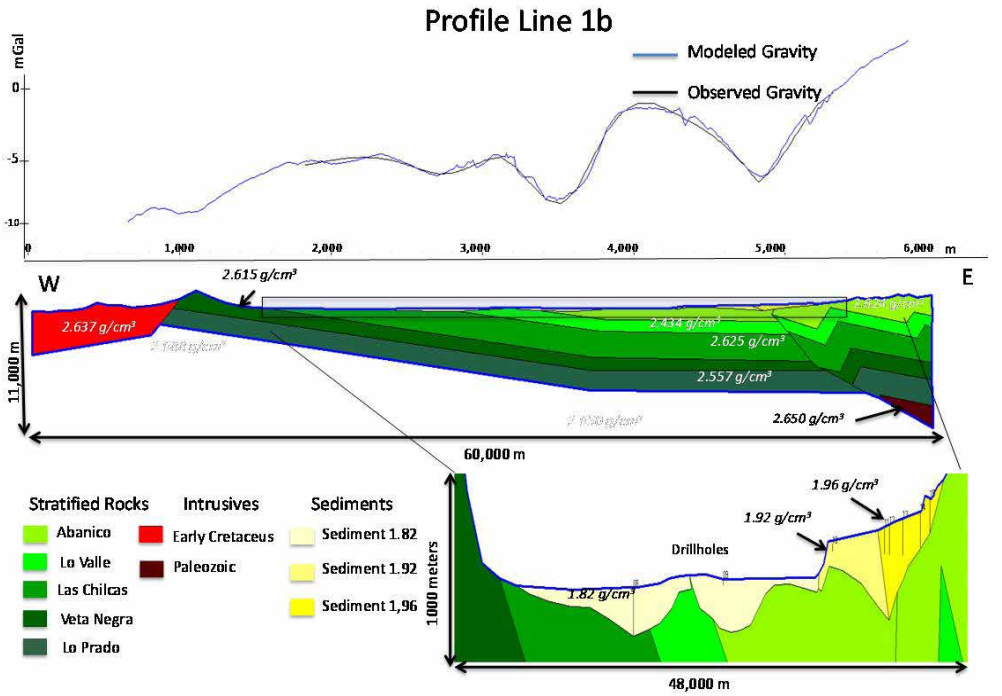

FIG. 9. Forward model of line 1b (see location in figure 7f). The observed gravity corresponds to Residual-2 field. In the zoom domain we show the basement and well constrains.

figure 11 we also show the correlation between 3D inversion model and 2.5D profile forward modeling (right panel). We see a good agreement between both methodologies, with a bit larger dispersion towards lower 3D depth estimates for deeper basement depths compared with the 2.5D solution. This is a likely result because 2.5D models tend to overestimate depths for 3D bodies.

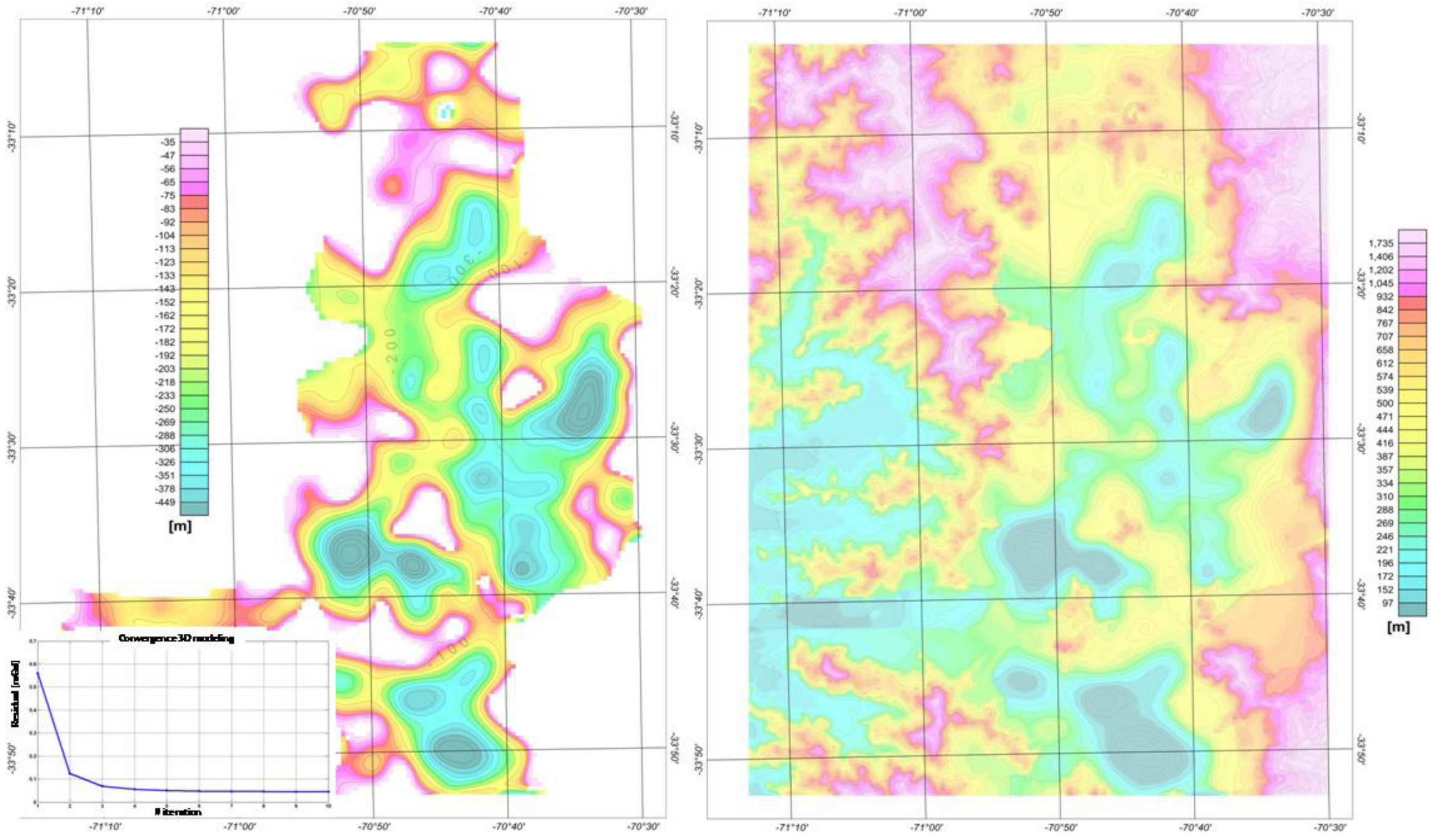

FIG. 10. **Left panel**: Depth to basement 3D inversion model; inside the lower left panel we include the convergence misfit for each iteration. **Right panel**: Relief topography after removing the sedimentary cover.

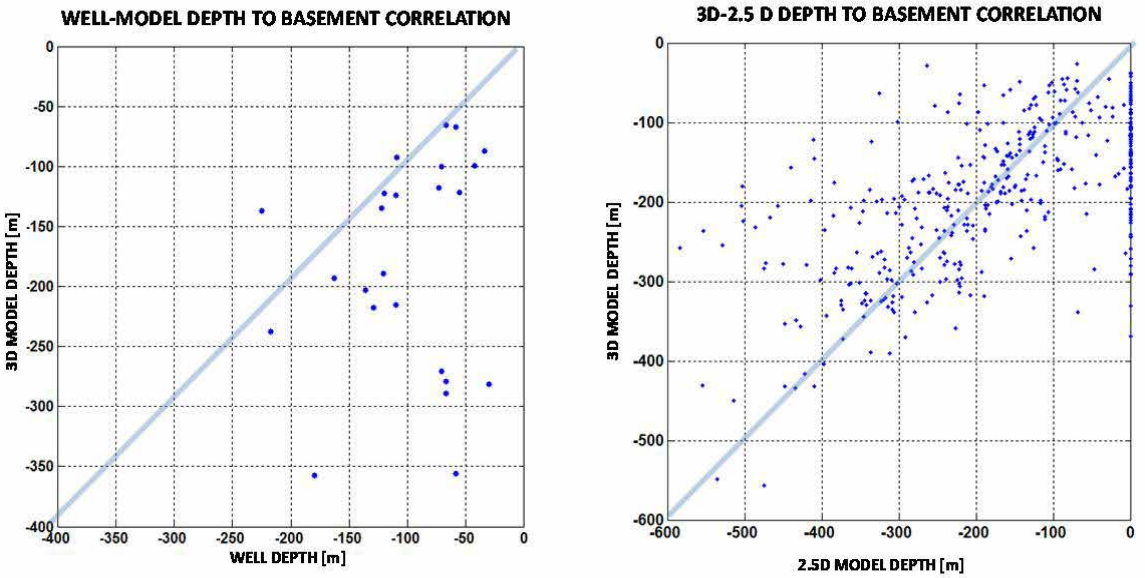

FIG. 11. Left panel: correlation of well depth and model 3D depth. Right panel: correlation of 3D and 2.5D depth to basement estimate.

7. Interpretation and Discussion

The depth to the basement in the Santiago Basin, allow us to address a series of connected issues that highlights the significance of this basin in terms of the geological evolution of this Andean segment, as well as geotechnical, hydrogeological, and seismic hazard implications described in the followings paragraphs.

7.1. How much time is required for the basin infill?

The depth to basement result obtained in this study (Fig. 10), indicates that the average thickness over the Santiago basin is 250 m, with a maximum depth of 640 m and a standard deviation of 120 m. We can distinguish 3 characteristic domains for depth to basement. The northern domain: Lampa, Batuco, and Colina villages, where depth to basin is lower than 150 m. The eastern-central domain: Chicureo and Pirque villages, and the main Santiago city. In this domain, that concentrates more than 3 million inhabitants, the average depth to basement is 300 m, with one of the three largest depocenters in the study area, that reach 630 m, located in the north-eastern side of this domain, the Las Condes depocenter. The last domain is located in the south-western flank of the study area: Peñaflor, Paine, Talagante, Buin, and Melipilla. The average depth to basement in this domain is slightly above the central domain, about 350 m. The remaining two larger depocenters are located in this domain, Peñaflor and Paine, with maximum depths of 630 m. In total we have a basin of ~2,400 square kilometers with an infilling volume of 600,000 cubic kilometers. This is a rather modest number, considering that the observed decennial and millennial erosion rate at this latitude is about 0.25 mm/yr (Carretier *et al.*, 2013). If this erosion rate remains fixed, the whole basin infill will be completed in 1 Ma. However is highly likely that a large percentage of the eroded material is finally fluvially-transported to the Chile-Perú trench. On the other hand, the high rate of erosion observed in the last millennial, largely conditioned by the last glaciation, is probably a transient behavior, and perhaps a more representative erosion rate for the Miocene uplift of the South-Central Andes, is 5-10 times slower (0.05-0.025 mm/yr). If that is the case, the basin infill in Santiago basin lasted 10-20 Ma, depending on the amount of material transported to the trench.

7.2. What is the geological genesis of the basin?

The basement topography presented in figure 10 (left panel) shows an important tectonic signal

of the basement, probably much less affected by erosional effects. In fact when we put together the sub-aerial relief and the hidden relief underneath the sedimentary cover a conspicuous suite of NW and NE trends that cross the entire study area is evident. This family of structures is complemented by some second order NS trends in the eastern flank of the study area. In figure 12a we make an interpretation of these structures, adding the crustal seismicity observed in the last 10 years (CHASE and ANILLO projects, (Pardo *et al.*, 2008, 2009); and NEIC and DGF data bases). Although location errors of these seismic events are not homogenous, we can be confident on horizontal errors smaller than 2-3 km (depth errors are in the order of 4-6 km, most likely, so it is fair to say they are crustal events). We can see that seismic activity is aligned mostly along some branches of the NW and NE trends interpreted from the basement topography map. The only seismic activity that departs from this behavior is the NS seismic alignment to the NW of Pirque, flanked by two NS trends, also interpreted in the basement topography map. As complementary information we include in figure 12 the regional magnetic field reduced to the pole (derived from the Magnetic Chart of Chile, (Sernageomin, 1986)). This map shows the same suite of NW and NE trends, as positive and/or negative magnetic anomalies. Magnetic response of sedimentary cover is normally considered negligible, so that these anomalies are probably representing magnetic contrast in basement rocks. On the other hand the magnetic susceptibility of basement outcrops (Fig. 5), show that Cretaceous and Cenozoic volcanic sequences are moderately-to-middle magnetized, and therefore the association of valley topography with negative magnetic signals is consistent with a negative magnetic contrasts in these domains. Thus, basement topography with NW and NE major trends is consistently supported by the observed seismicity and magnetic signal of basement origin. These major trends exceeds the study area, and in fact they have been recognized in this zone from different lines of reasoning, in the eastern High Andes (*e.g.,* Rivera and Cembrano, 2000; Piquer, 2014) and in the western Cordillera de la Costa range (*e.g.*, Yáñez *et al.*, 1998, 2002). These lithospheric-scale structures are represented schematically in figure 12b, whiting the context of the present study. Comparing the interpreted structural pattern (Fig. 12a) with the regional scale context (Fig. 12b), we can appreciate that at least the first order NE and NW structures share a common signature, and likely origin. The origin of these lithospheric-scale structures is not fully understood yet, however they are controlling Mesozoic deposits (Rivera and Cerda, 2012), and probably linked to the Triassic rifting of the Andean Margin (Fock *et al.*, 2006). The previous line of reasoning suggest that the interpreted tectonic lineaments in the basin probably belongs to a much broader-scale structures with a long-lived tectonic control from pre-Andean times. The first order role of thrust faulting in the eastern border of the basin as a driven mechanism for the Andean uplift (*e.g.,* the San Ramón thrust fault, (Armijo *et al.*, 2010)), is only partially supported by this tectonic intepretation. In fact, the large north east depocenter of Las Condes is shorter than 10 km long, and seems to be controlled by a combination of NE and NS structures. The southern, and largest (~20 km), eastern flank of the basin doesn't show any relevant depocenter at the trace of the San Ramón fault trace. Thus, the absence of large sedimentary deposits in the footwall of the thrust fault suggest a secondary role in the uplift evolution of this segment of the Andes. The NS seismic activity, described previously, to the west of San Ramón Fault, has been studied in detail by (Pardo *et al.*, 2009), concluding that this seismicity is below 10 km depth, coinciding with the western border of the dense mid-crustal block, but without any clear connection with high angle shallower thrust faults. Even though the genesis of the basin is most likely older than the Andean orogenesis, the structural control is still active as becomes evident from the seismic activity (Fig. 12). This seismicity represents the deformation of the continental margin during the inter-seismic period of the Nazca-South America convergence.

7.3. Is there any role of the sedimentary thickness/density on the seismic amplification of the basin?

Spectral ratio between horizontal and vertical micro-vibrations (H/V) has been used successfully estimating the dynamic response of soils through the fundamental frequency of resonance (Nakamura, 1989, 2000). This approach has been applied in recent years in Santiago basin (Leyton *et al.*, 2010;

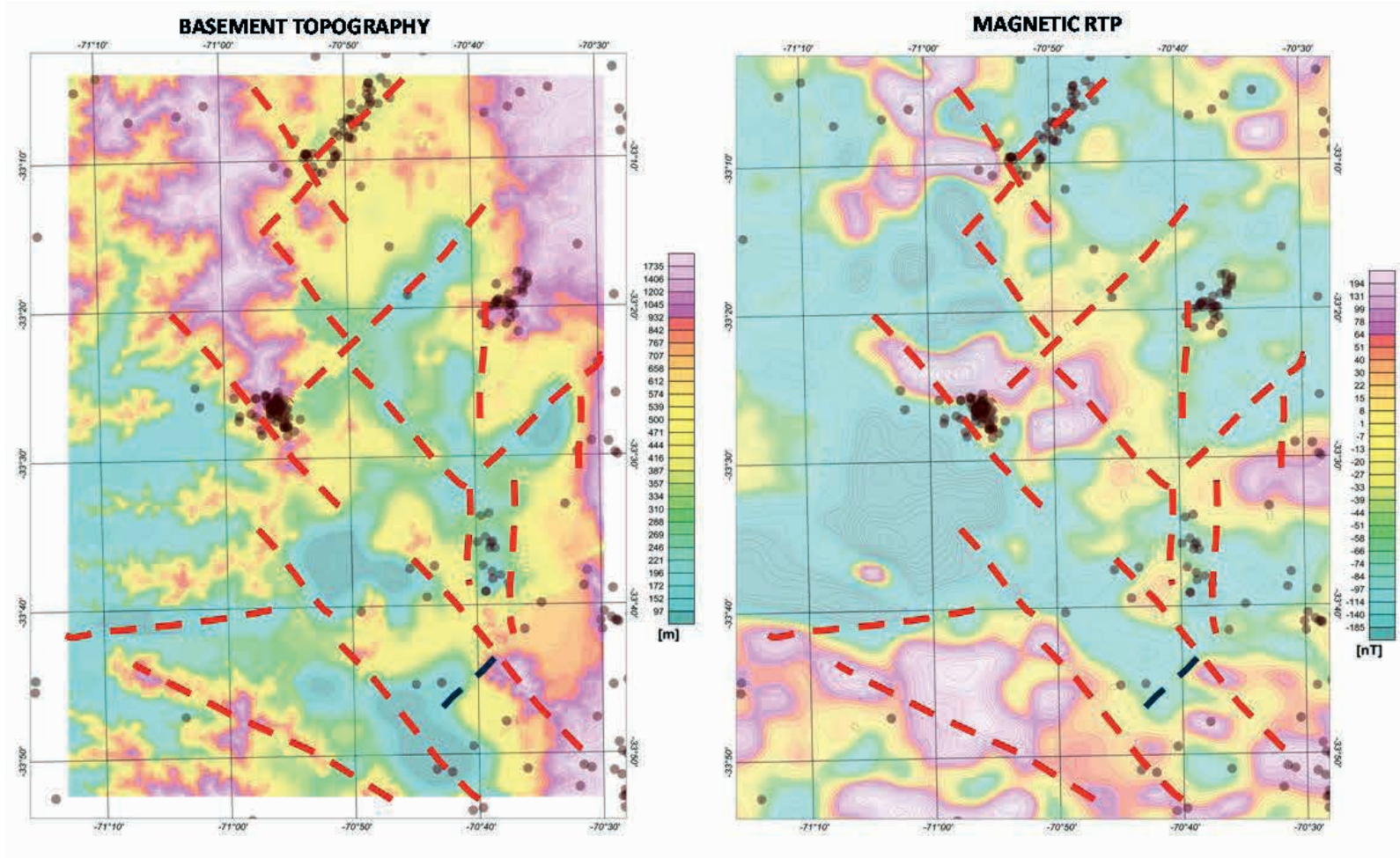

FIG. 12. **A.** Left panel: Basement topography underlying the structural interpretation (red segmented lines), and the crustal seismic activity (grey dots). Right panel: magnetic field reduced to the magnetic pole of the Magnetic Chart of Chile (Sernageomin, 1986). Structural interpretation is based on the depth-to-basement map. **B.** Structural interpretation of figure 12a (red segmented lines over a red box) placed in a regional context. Schematic structural context (blue lines) derived from different studies (*e.g.*, Rivera and Cembrano, 2000; Piquer, 2014; Yáñez *et al.*, 1998, 2002). As a background, the natural crustal seismicity (CHASE and ANILLO projects, (Pardo *et al.*, 2008, 2009); and NEIC and DGF data bases), and the Geological map 1:1,000,000 (Sernageomin, 2002).

Pasten, 2007; Bonnefoy-Claudet *et al.*, 2009). A compilation based on these results, and unpublished data from F. Leyton, personal communication, 2014, is presented in figure 13 in terms of fundamental frequency (F_O) and maximum peak amplitude (A_O). In theory, the peak amplitude (A_O) is proportional to the acoustic impedance ratio of the basement (sub-index 2) and cover (sub-index 1) $\left(A_o = \frac{v_2 - \rho_2}{v_1 - \rho_1}\right)$, and the fundamental frequency (F_O) develops when the wavelength of the seismic wave is four times the layer thickness (b_o) $\left(b_o = \frac{v_1}{4F_o}\right)$, (*e.g.*, Anderson, 2007). If these relations hold, then correlation between F_O and the depth to basement will be high as well as the relation between the density of the sedimentary cover and the peak amplitude (A_O). If we look at this correspondence in figure 13, we see that at first glance A_O and density do share a reasonable good correlation, with high amplitude values when density of sedimentary cover is low (in the northern part of the study area). However, the correlation between depth to basement and F_O is more ambiguous, although some correspondence is observed between larger depth to basement and low fundamental frequency as expected. As has been pointed out by (Bonnefoy-Claudet *et al.*, 2009), these discrepancies can be attributed to topographic effects (non-flat contact between the sedimentary cover and the basement), and impedance contrast between sedimentary cover and some compacted sedimentary sequence at intermediate depths. In order to test this hypothesis we analyze the correlation between amplitude and theoretical impedance, as well as the gravity-derived depth to basement and the predicted depth from the fundamental frequency relationship $\left(b_o = \frac{v_1}{4F_o}\right)$ (Fig. 14). Implicit in this figure is the estimate of the shear wave velocity of the sediment cover, computed from the empirical Vs-density relationship for unconsolidated sediments (Ojha and Sain, 2012):

$$V_s\left[\frac{m}{s}\right] = \left[\frac{\rho[\frac{gr}{cc}]}{2.02}\right]^8$$

Looking first at the peak-amplitude/impedance-contrast, we see that a reasonable good correlation is observed, confirming the qualitative correspondence at a map view (Fig. 13). As expected, the large amplitude values are obtained when depth to basement distance is short. This good correspondence is achieved for a basement impedance of 3,460 [Kg/(m^{2}s)]. This rather low number is compatible with a density of 2,100 [Kg/m^3] and shear wave velocity of 1,400 [m/s]. These numbers are consistent with relatively compacted gravel sediments (*e.g.*, Telford and Sheriff, 1990). So the resonance depth in Santiago basin is lower than the depth to basement computed from gravity 3D inversion. This inference is partially supported when we look at the correlation of the depth to basement and the F_O-derived depth (Fig. 14, right panel). In fact, more than half of the points lay on the lower quadrant, where gravity-derived depths are larger than predicted values. Besides the likely bad identification of peak frequency in the low frequency spectrum, the observed large scattering in the correlations might be attributed to the lack of horizontal basement relief (topographic effects). In order to test this hypothesis we plot the same relations previously described, but colored in terms of the absolute gradient of the basement relief (lower panel of figure 14). We clearly see that observation points where basement slope is larger, have a relevant contribution to the observed scattering. This observation points towards the relevant role of 2D and 3D basement relief changes on the soil amplification, as postulate previously by (Bonnefoy-Claudet *et al.*, 2009).

7.4. Is there any chance for low enthalpy geothermal potential of the basin?

Low enthalpy geothermal energy for district heating consists in heat exchange with the ground, then the implications of the Santiago basin geometry in this renewable energy and its management is related directly to the effect of the basin geometry in groundwater flow. Several studies indicate that a high heat source increases the efficiency of a Geothermal Heat Pump in heating mode (Florides *et al.*, 2011) and as the heat in the sedimentary infill is carried by the groundwater flow, the direction of groundwater linked with the interconnection between sub-basins or possible barriers into the Santiago basin are useful to infer where the heat is moving. Besides the utilization of this geothermal resource produces thermal affected zones in subsurface, which will move with the groundwater flow (Lo Russo *et al.*, 2012) then the basin geometry will be helpful to infer the affected areas by the exchange of heat with the subsurface. Present static level of well data base from DGA is presented in figure 15 in companion to gravity-derived-depth to basement. There is some reasonable good correlation

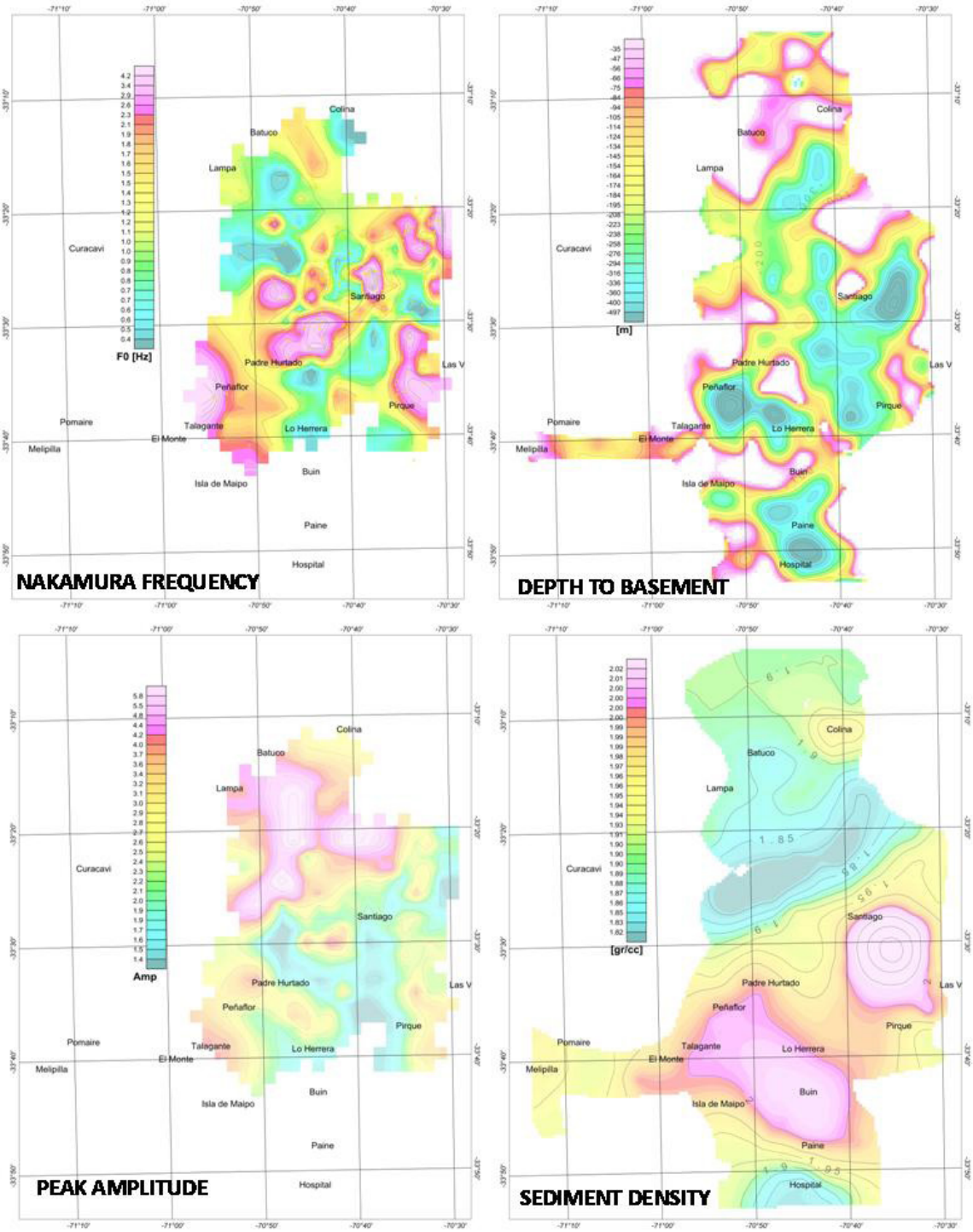

FIG. 13. Fundamental frequency F_0 (left upper panel), and peak amplitude (A_0) (left lower panel). Yellow dots are the sites used for the interpolation of the mechanic soil response. In the right panel we include the sedimentary density (lower right panel), and the depth to basement (upper right panel).

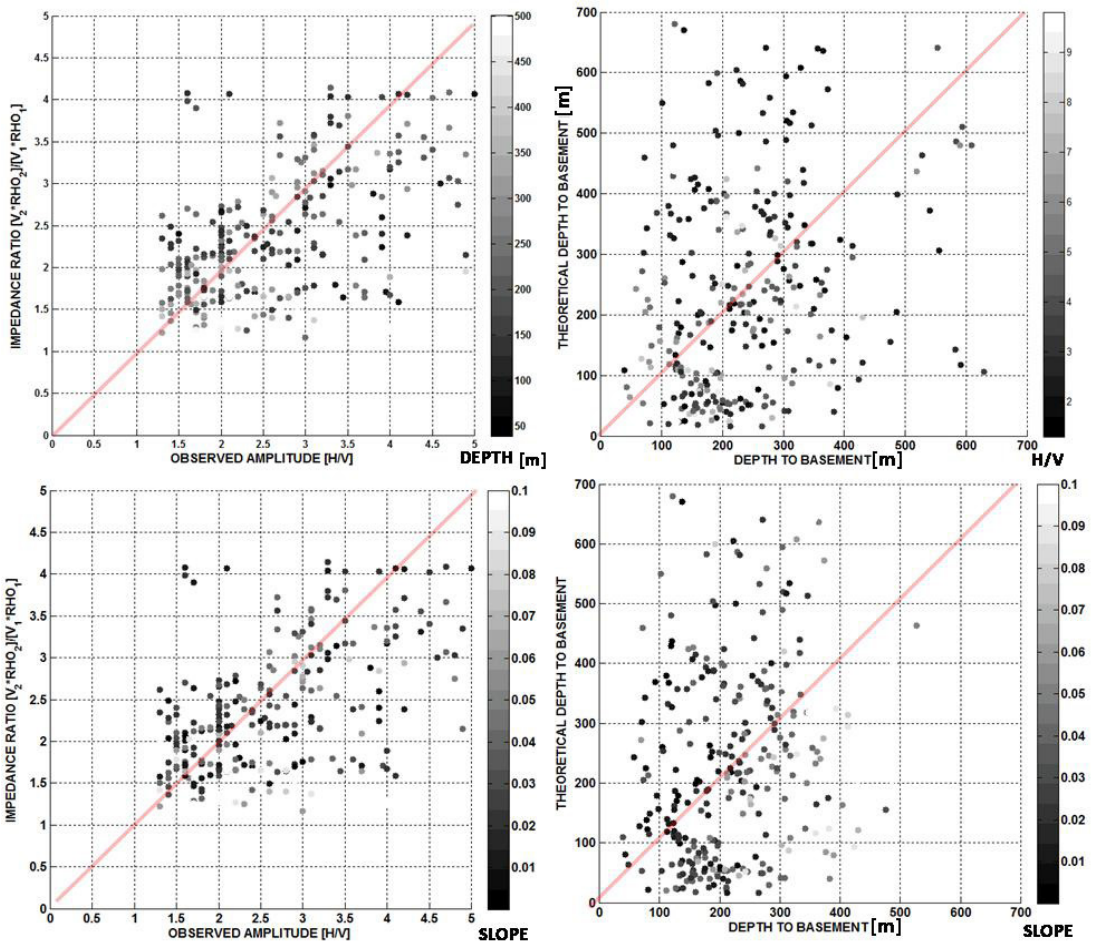

FIG. 14. Correlation between observed amplitude (H/V) and impedance ratio between basement and cover (left panel), and gravity-derived depth to basin and theoretical depth to basement using the $b_o = \frac{v_1}{4F_o}$ relation (right panel). Upper left panel colors are a function of the computed depth to basement. Color in the upper rignt panel is a function of the H/V amplitude ratio. Finally, the color in both lower panels is a function of the basement slope in each measured point.

between deeper static level and the deeper part of the basin in the eastern central domain. This is the expected behavior for an unconfined aquifer with an increased gravitational recharge from the east (*e.g.*, Töth, 2009). This correlation becames more clear when we look at AA' section of figure 16, with static levels in excess of 100 m in the eastern part. This first order correlation implies that the location of the deeper part of the eastern central domain derived form gravity measurements is consistent with the water table behavior there. In this sector we have also the fortune to have acces to the only two TEM soundings (Transient Domain Electromagnetic). These soundings (shown in figure 16), maps the electrical resistivity vertically, low resistivity (below 10 ohm-m) means presence of water, and the opposite implies dry sediments and/or basement rocks. Looking at the TEM results, we see that the low resistivity domain match perfectly the static level and the basement, suggesting in fact that the whole basin is saturated with water, and also validating the depth estimate form the gravimetric study with an independent methodolgy, at least in this domain. In contrast, the south-western domain shows a very shallower static level (0-5 m), as a result of the lower topography that almost coincide with the freatic level. The presence of two sub-basins (the east central domain and the southern domain), likely independents and with different hydraulic behaviors, has implications in terms of the potential use for

low enthalpy geothermal use. In theory, a column of 500 m allows an increment in temperature to the ranges required for low enthalpy applications (~20 °C), considering geothermal gradients and heat production of basement rocks in Central Chile (Suárez *et al*., 2014). However direct measurements in Santiago Basin (Muñoz *et al*., 2012) indicates that well temperature gradients are generally lower than the requiered numbers. This behavior appears to be mostly controlled by the strong horizontal glacier/river-derived ground water advection mainly produced by the watershed recharge in the apical part of the Maipo river alluvial fan. Secondarily, the rapid changes in the hydraulic conductivity related to the large variability of the sedimentary infill, produces relatively high groundwater velocities and therefore a short residence time in the basin, limiting its heating (Morales, 2002). A very sismplistic thermal advection flow model (heat equation with and advective horizontal velocity component, *e.g*., Turcotte and Schubert, 2014) is presented in figure 17, trying to simulate different scenarios depending on the flow pattern and temperature at the cold eastern recharge zone (parametrized by flow velocity, thermal gradient, and a constant thermal difussivity of $6*10^{-7}$ m^2/s, appropriate for saturated sands (Thomson, 2010). The cold inflow from the east is simulated using different thermal gradients there. A value of 30°/km implies no cold plumes advected down the stream, whereas a 6°/km implies a great contribution from cold waters. As expected for relatively large flow velocities (20 cm/day), the advection of cold water downstream produce a reduction of the thermal gradient, almost constant throughout the basin, reducing the temperature at middle depth to more than 50%. For a relatively slower flow velocities (4 cm/day), the reduction in the thermal gradient open some chances for higher temperatures, in particular in the western parts of the basin. From this very simplistic numerical analysis it becomes evident that chances for low enthalpy geothermal viable scenarios are restricted to the southern sub-basin. This sub-basin, away from the cold source and likely with smaller flow rates, can sustain larger residence time within the basin. Given the fact that the great majority of thermal gradient observations in the basin are related to shallow wells (less than 100 m), still there are chances to find the appropriate temperatures for low enthalpy applications in the deeper parts, in particular in the southern sub-basin.

8. Conclusions

In this study we estimate the depth to basement in Santiago Basin using the gravity-method tool. This interpretation has been constrained by sediment and hard rock petrophysical measurements, in distinctive parts of the basin and periphery. In addition we validate the depth to basement with well soundings depth measurements (minimum and basement intersection). Gravimetric modeling effort included three steps, regional estimate, 2.5D forward modeling, and 3D inversion modeling. Regional gravity in the study area is composed by heterogeneous multi source components of different wavelength and depth to the source. Large and deep-scale sources, crustal roots and mid-crustal dense blocks were directly modeled from regional estimates. Heterogeneous basement response is directly modeled within the 2.5D forward models of 10 E-W lines. Final 3D inversion model is computed over a residual gravity field, in which the basement heterogeneous sources modeled in the 2.5D stages has been removed.

Depth to basement model results shows that the Santiago basin has a mean depth thickness of 300 m, with three major depocenters in excess of 500 m of sedimentary cover. According to the estimates of erosion rate in Central Chile we conclude that the basement infill last between 10-20 Ma, depending on the persistence of the erosion rate and the ratio of sedimentary deposition/transport towards the deep ocean.

Basement relief, integrated with surface topography, natural crustal seismicity, magnetic field, and regional-scale major structures, are consistent with a basin genesis controlled by pre-existing features that pre-date the Andean cycle. Natural seismicity, mostly concentrated along these first order structures of NW and NE orientation, suggest that the present-day inter-seismic deformation is mostly accommodated there. NS features in the eastern border of the basin are limited in extension and probably of second order in terms of Andean deformation.

Comparing the dynamic response of soils show that peak spectrum amplitude is directly correlated with the basement to cover impedance ratio, and the natural frequency of resonance is moderately well correlated with the depth to basement estimate. The average peak spectrum amplitude is consistent with a basement impedance more affine with a compacted sedimentary cover than a hard rock or

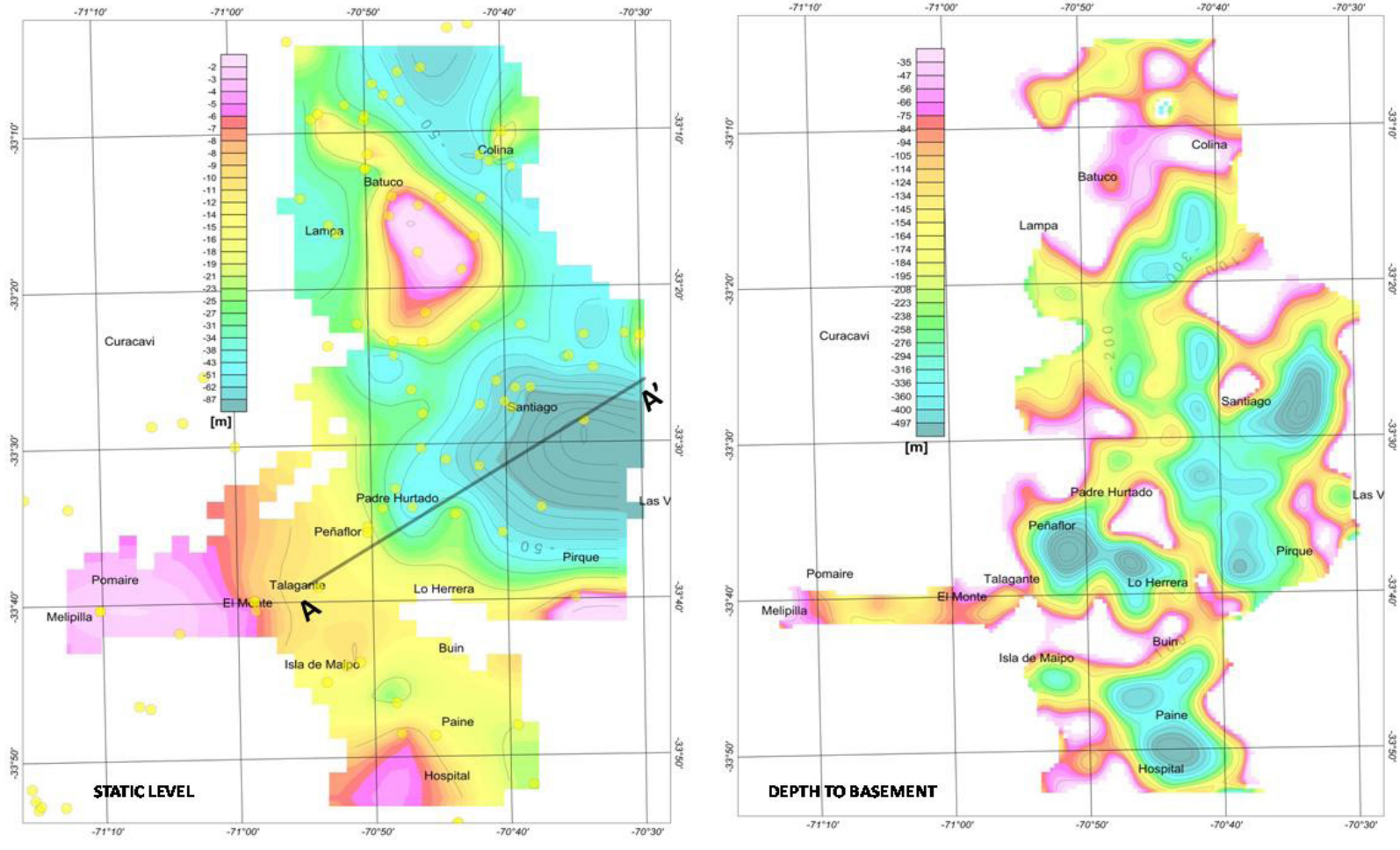

FIG. 15. Static level (left panel). Included in this panel the observations points (yellow circles), and the AA' profile locations. In the right panel the depth to basement.

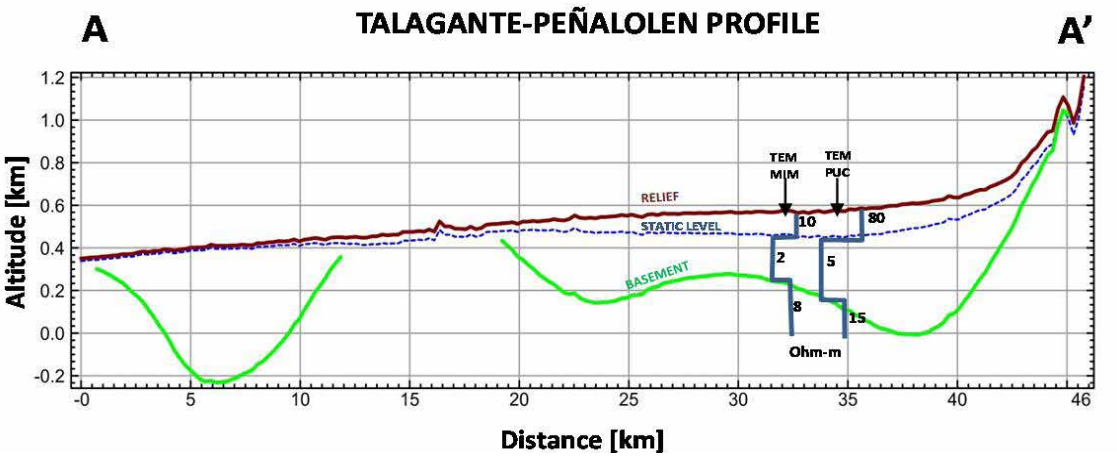

FIG. 16. Profile of basement topography (green line) and static level (dotted blue line) (see location in figure 15). The TEM soundings of MIM and PUC are included in blue heavy lines. Resistivity depth profiles are in log (ohm-m) scaling (scale included ate the bottom).

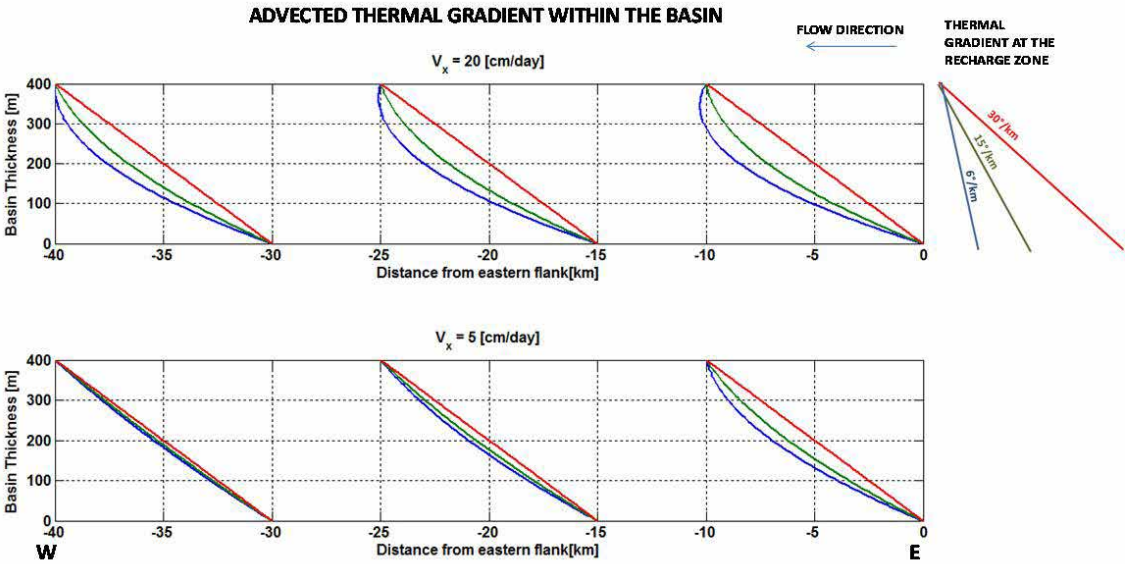

FIG. 17. Simulation of thermal gradient forced by a ground water flow from the E, with different flow rates (lower panel: 4 [cm/day]; upper panel: 20 [cm/day]), and thermal gradient in the eastern recharge zone (red: 30°/km, green: 15°/km, blue: 6°/km). Thermal gradient profiles are simulating the western, central, and eastern domain of the basin in figure 16.

basement response. This observation can explain why the fundamental frequency/depth to basement correspondence is not fully sustained because both quantities are probably mapping different depths horizons, with a resonance depth a bit shallower that the depth to basement. Discrepancies are larger when the slope of the basement is higher, pointing towards 2D and 3D effects not well resolved by the 1D theoretical assumptions.

The static level depth is deeper in the eastern front of the basin, in good agreement with the larger depth to basement there, as a result of a gravitationally-driven flow. Water table depth and aquifer thickness in this domain is well supported by TEM vertical

soundings, confirming that sedimentary sequence is, to first order, fairly homogenous. On the other hand, chances to use the aquifers for low enthalpy geothermal applications appears to be limited to the deeper parts of the southern sub-basin.

Acknowledgments

FONDAP-CONICYT project Nº 15090013 (Andean Geothermal Centre of Excellence), Renewable Energy Division of the Chilean Energy Ministry and the Department of Geology of the Universidad de Chile. In addition, seismic compilation has been provided by CHASE and ANILLO projects supported by Fondecyt 1050758, IRD-Francia, Anillo ACT-18. Gravity survey has been partially supported by FONDAP-CONICYT project (CIGIDEN, Centro Nacional de Investigación para la Gestión Integrada de Desastres Naturales). We also would like to thank Dr. Felipe Leyton who kindly provided his dynamic soil response data base, and Mr. Tony Rojas from TRV who provided the TEM studies in Santiago Basin. Very stimulating discussions with Isabel Santibañez, Sebastien Carretier, and José Muñoz, improve our knowledge and the discussion.

References

Anderson, D.L. 2007. New Theory of the Earth. Cambridge University Press: 384 p. New York.

Araneda, M.; Avendaño, M.; Merlo, C. 2000. Modelo gravimétrico de la Cuenca de Santiago, etapa III final. *In* Congreso Geológico Chileno, No. 9, Actas 2: 404-408. Puerto Varas.

Armijo, R.; Rauld, R.; Thiele, R.; Vargas, G.; Campos, J.; Lacassin, R.; Kausel, E. 2010. The West Andean Thrust, the San Ramón Fault, and the seismic hazard for Santiago, Chile. Tectonics 29 (2): TC2007. doi: 10.1029/2008TC002427.

Bonnefoy-Claudet, S.; Baize, S.; Bonilla, L.F.; Berge-Thierry, C.; Pasten, C.; Campos, J.; Volant, P.; Verdugo, R. 2009. Site effect evaluation in the basin of Santiago de Chile using ambient noise measurements. Geophysical Journal International 176 (3): 925-937.

Bosch, A. 2014. Gravedad Cuenca de Santiago. Professional degree dissertation. Pontificia Universidad Católica de Chile: 59 p.

Brantt, C. 2011. Microzonificación sísmica del sector sur poniente de Santiago, comunas Buin y Paine. Bachelor Thesis (Unpublished), Universidad de Chile: 139 p.

Carretier, S.; Regard, V.; Vassallo, R.; Aguilar, G.; Martinod, J.; Riquelme, R.; Pepin, E.; Charrier, R.; Hérail, G.; Farías, M. 2013. Slope and climate variability control of erosion in the Andes of central Chile. Geology 41 (2): 195-198.

Charrier, R.; Baeza, O.; Elgueta, S.; Flynn, J.J.; Gans, P.; Kay, S.M.; Muñoz, N.; Wyss, A.R.; Zurita, E. 2002. Evidence for Cenozoic extensional basin development and tectonic inversion south of the flat-slab segment, southern Central Andes, Chile (33-36ºS). Journal of South American Earth Sciences 15 (1): 117-139.

Charrier, R.; Bustamante, M.; Comte, D.; Elgueta, S.; Flynn, J.J.; Iturra, N.; Muñoz, N.; Pardo, M.; Thiele, R.; Wyss, A.R. 2005. The Abanico extensional basin: Regional extension, chronology of tectonic inversion and relation to shallow seismic activity and Andean uplift. Neues Jahrbuch Fur Geologie Und Palaontologie-Abhandlungen 236 (1-2): 43-78.

Charrier, R.; Farías, M.; Maksaev, V. 2009. Evolución tectónica, paleogeográfica y metalogénica durante el Cenozoico en los Andes de Chile norte y central e implicaciones para las regiones adyacentes de Bolivia y Argentina. Revista de la Asociación Geológica Argentina 65 (1): 5-35.

DGA, 2000. Modelo de Simulación Hidrológico Operacional: Cuencas de los ríos Maipo y Mapocho. Ayala, Cabrera y asociados. Dirección General de Aguas, Ministerio de Obras Públicas, Series SIT No. 62 (8v): 87 p.

Dragicevic, M. 1970, Carta gravimétrica de los Andes meridionales e interpretación de las anomalías de gravedad de Chile Central. Departamento de Geofísica, Universidad de Chile: 42 p.

Falcón, E.; Castillo, O.; Valenzuela, M. 1970. Hidrogeología de la Cuenca de Santiago. Corporación de Fomento de la Producción, Departamento de Recursos Hidráulicos: 46 p. Santiago.

Florides, G.A.; Pouloupatis, P.D.; Kalogirou, S.; Messaritis, V.; Panayides, I.; Zomeni, Z.; Partasides, G.; Lizides, A.; Sophocleous, E.; Koutsoumpas, K. 2011. The geothermal characteristics of the ground and the potential of using ground coupled heat pumps in Cyprus. Energy 36 (8): 5027-5036. doi: 10.1016/j.energy.2011.05.048.

Fock, A. 2005. Cronología y tectónica de la exhumación en el Neógeno de los Andes de Chile central entre los 33° y los 34°S. Tesis de Doctorado (Unpublished), Departamento de Geología, Universidad de Chile: 235 p.

Fock, A.; Charrier, R.; Farías, M.; Muñoz, M. 2006. Fallas de vergencia oeste en la Cordillera Principal de Chile Central: Inversión de la cuenca de Abanico (33°-34°S). Revista de la Asociación Geológica Argentina, Publicación Especial 6: 48-55.

Fuentes, F.; Vergara, M.; Aguirre, L.; Féraud, G. 2002. Relaciones de contacto de unidades volcánicas terciarias

de los Andes de Chile central (33°S): una reinterpretación sobre la base de dataciones $^{40}Ar/^{39}Ar$. Revista Geológica de Chile 29 (2): 207-225. doi: 10.5027/andgeoV29n2-a04.

Gálvez, C. 2012. Microzonificación sísmica en los sectores de Lampa y Batuco, Región Metropolitana, Chile. Bachelor Thesis (Unpublished), Universidad de Chile: 189 p.

Gana, P.; Wall, R.; Gutiérrez, A. 1996. Mapa geológico del área Valparaíso-Curacaví, Regiones de Valparaíso y Metropolitana. Servicio Nacional de Geología y Minería, Mapas Geológicos 1: 20 p., 1 mapa 1:100.000. Santiago. .

Godoy, E.; Lara, L. 1994. Segmentación estructural andina a los 33°-34°: nuevos datos en la Cordillera Principal. *In* Congreso Geológico Chileno, No. 7, Proceedings 2: 1344-1348. Concepción.

INE. 2002. Censo, 2002. http://www.ine.cl/cd2002/sintesiscensal.pdf, INE (última visita 02-04-2015).

Jara, P.; Charrier, R. 2014. Nuevos antecedentes estratigráficos y geocronológicos para el Meso-Cenozoico de la Cordillera Principal de Chile entre 32° y 32°30'S: Implicancias estructurales y paleogeográficas. Andean Geology 41 (1): 174-209. doi: 10.5027/andgeoV41n1-a07.

Jara, P.; Likerman, J.; Cristallini, E.; Ghiglione, M.; Pinto, L.; Charrier, R.; Jara, C. 2012. Analogue models of basins affected by differential deformation in extensional and compressional regimes. *In* Congreso Geológico Chileno, No. 13, Actas: 302-304. Antofagasta.

Kausel, E. 1959. Levantamiento gravimétrico de la Cuenca de Santiago. Professional degree dissertation. Universidad de Chile: 104 p.

Kay, S.M.; Godoy, E.; Kurtz, A. 2005. Episodic arc migration, crustal thickening, subduction erosion, and magmatism in the south-central Andes. Geological Society of America, Bulletin 117 (1-2): 67-88.

Leyton, F.; Sepúlveda, S.A.; Astroza, M.; Rebolledo, S.; González, L.; Ruiz, S.; Foncea, C.; Herrera, M.; Lavados, J. 2010. Zonificación Sísmica de la cuenca de Santiago, Chile. *In* Congreso Chileno de Sismología e Ingeniería Antisísmica, No. 10, Universidad de Chile: 22-27. Santiago.

Linsley, R.K.; Kohler, M.A.; Paulhus, J. 1982. Hydrology for Engineers (McGraw-Hill, I.; editor). McGraw-Hill Series in Water Resources and Environmental Engineering: 508 p.

Morales, F. 2002. Definición de Acuíferos en la cuenca del río Maipo, Bachelor Thesis (Unpublished), Universidad de Chile: 113 p.

Mues-Schumacher, U.; Schumacher, R.; Viereck-Götte, L.G.; Lepetit, P. 2004. Areal Distribution and Bulk Rock Density Variations of the Welded Incesu Ignimbrite, Central Anatolia, Turkey. Turkish Journal of Earth Sciences 13: 249-267.

Muñoz, M.; Fuentes, F.; Vergara, M.; Aguirre, L.; Nyström, J.O.; Féraud, G.; Demant, A. 2006. Abanico East Formation: petrology and geochemistry of volcanic rocks behind the Cenozoic arc front in the Andean Cordillera, central Chile (33°50'S). Revista geológica de Chile 33 (1): 109-140. doi: 10.5027/andgeoV33n1-a05.

Muñoz, M.; Flores-Aqueveque, V.; Gramusset, A.; Vargas, G.; Rebolledo, S.; Sepúlveda, S.; Parada, M.A.; Morata, D. 2012. Parámetros termales en el subsuelo de la cuenca de Santiago: Metodología y primeros resultados. *In* Congreso Geológico Chileno, No. 13: 432-434. Antofagasta.

Nakamura, Y. 1989. A method for dynamic characteristics estimation of subsurface using microtremor on the ground surface. Railway Technical Research Institute (RTRI), Quarterly Reports 30 (1): 25-30.

Nakamura, Y. 2000. Clear identification of fundamental idea of Nakamura's technique and its applications. *In* Proceedings of the world conference on earthquake engineering, No. 12: 8 p. Auckland.

Nyström, J.O.; Vergara, M.; Morata, D.; Levi, B. 2003. Tertiary volcanism during extension in the Andean foothills of central Chile (33°15'-33°45'S). Geological Society of America, Bulletin 115: 1523-1537.

Ojha, M.; Sain, K. 2012. Empirical trends of velocity-porosity and velocity-density in shallow sediment in Kerala-Konkan Basin on the west cost of India. *In* Biennial International Conference and Exposition on Petroleum Geophyiscs, No. 9: p. 444. Hyderabad.

Pardo, M.; Vera, E.; Monfret, T.; Yáñez, G. 2008. Crustal seismicity and 3D seismic wave velocity models in the Andes cordillera of Central Chile (33°-34.5°S) from local earthquakes. *In* International Symposium on Andean Geodynamics, No. 7. Extended Abstracts: 377-380. Nice.

Pardo, M.; Vera, E.; Yáñez, G.; Monfret, T. 2009. Tomografía Sísmica Bajo los Andes de Chile Central (33°-34.5°S): Implicaciones Sismotectónicas. *In* Congreso Geológico Chileno, No. 12, S9-067: 1-4. Santiago.

Pardo-Casas, F.; Molnar, P. 1987. Relative motion of the Nazca (Farallon) and South American plates since Late Cretaceous time. Tectonics 6 (3): 233-248.

Pasten, C. 2007. Respuesta sísmica de la cuenca de Santiago. M.Sc. Thesis (Unpublished), Universidad de Chile: 259 p.

Piquer, J. 2014. Structural architecture of the Abanico Basin, Andes of Central Chile: its relation with Mio-Pliocene magmatism and porphyry Cu-Mo deposits. *In*

Geological Society of Australia, SGTSG Conference: p. 72. Thredbo.

Plouff, D. 1976. Gravity and magnetic fields of polygonal prisms and application to magnetic terrain corrections. Geophysics 41 (4): 727-741.

Poffijn, A.; Berkvens, P.; Vanmarcke, H.; Bourgoignie, R. 1988. On the exhalation and diffusion characteristics of concrete. Radiation Protection Dosimetry 24 (1-4): 203-206.

Rauld, R. 2011. Deformación cortical y peligro sísmico asociado a la Falla San Ramón en el frente cordillerano de Santiago, Chile central (33ºS). Ph.D. Thesis (Unpublished), Universidad de Chile: 265 p.

Rivera, O.; Cembrano, J. 2000. Modelo de Formación de Cuencas Volcano-Tectónicas en Zonas de Transferencia Oblicuas a la Cadena Andina: El Caso de las Cuencas Oligo-Miocenas de Chile Central y su Relación con Estructuras WNW-NW (33º00'-34º30' LS). *In* Congreso Geológico Chileno, No. 9: 631-636. Puerto Varas.

Rivera, O.; Cerda, A. 2012. Los Pórfidos Cupríferos de Chile Central: Significado de Estructuras Translitosféricas y Anomalías Gravimétricas en la Metalogénesis Andina. *In* Congreso Geológico Chileno, No. 13: 2-4. Antofagasta.

Lo Russo, S.; Taddia, G.; Verda, V. 2012. Development of the thermally affected zone (TAZ) around a groundwater heat pump (GWHP) system: a sensitivity analysis: Geothermics 43: 66-74.

Sellés, D. 1999. La Formación Abanico en el Cuadrángulo Santiago (33°15'-33°30'S; 70°30'-70°45'O) Chile central: Estratigrafía y geoquímica. M.Sc Thesis (Unpublished), Universidad de Chile: 154 p.

Sellés, D.; Gana, P. 2001. Geología del área Talagante-San Francisco de Mostazal, Regiones Metropolitana de Santiago y del Libertador General Bernardo O'Higgins. Servicio Nacional de Geología y Minería, Serie Geología Básica 74: 30 p., escala 1:100.000. Santiago.

Sernageomin. 1986. Hoja Santiago. Servicio Nacional de Geología y Minería, Serie Carta Magnética de Chile 19, 1 mapa escala 1:250.000. Santiago.

Sernageomin. 2002. Mapa Geológico de Chile 1:1.000.000. Servicio Nacional de Geología y Minería, Carta Geológica de Chile, Serie Geología Básica 75, 1 mapa en 3 hojas.

Spector, A.; Grant, F.S. 1970. Statistical models for interpreting aeromagnetic data. Geophysics 35 (2): 293-302.

Stern, C.R.; Amini, H.; Charrier, R.; Godoy, E.; Hervé, F.; Varela, J. 1984. Petrochemistry and age of rhyolitic pyroclastics flows which occur along the drainage valleys of the Río Maipo and Río Cachapoal (Chile) and the Río Yaucha and Río Papagayos (Argentina). Revista Geológica de Chile 23: 39-52. doi: 10.5027/andgeoV11n3-a03.

Suárez, F.; Sotomayor, R.; Oportus, T.; Yáñez, G.; Hausner, M.B.; Muñoz, M. 2014. Complementando el conocimiento hidrogeológico mediante sistemas distribuidos de temperatura. *In* Congreso Latinoamericano de hidrogeología, No. 12: 9 p. Santiago.

Tassara, A.; Yáñez, G. 2003. Relación entre el espesor elástico de la litósfera y la segmentación tectónica del margen andino (15-47°S). Revista Geológica de Chile 30 (2): 159-186. doi: 10.5027/andgeoV30n2-a02.

Tassara, A.; Götze, H.; Schmidt, S.; Hackney, R. 2006. Three dimensional density model of the Nazca plate and the Andean continental margin. Journal of Geophysical Research: Solid Earth 111 (B09404). doi: 10.1029/2005JB003976.

Telford, W.M.; Geldart, L.P.; Sheriff, R.E. 1990. Applied Geophysics. Cambridge University Press: 770 p.

Thomson, J. 2010. Observations of thermal diffusivity and a relation to the porosity of tidal flat sediments. Journal of Geophysical Research 115 (6): p. C05016. doi: 10.1029/2009JC005968.

Töth, J. 2009. Gravitational systems of groundwater flow: theory, evaluation, utilization. Cambridge University Press: 297 p.

Turcotte, D.L.; Schubert, G. 2014. Geodynamics third edition. Cambridge University Press: 623 p.

Wall, R.; Gana, P.; Gutiérrez, A. 1996. Mapa geológico del área de San Antonio-Melipilla, regiones de Valparaíso, Metropolitana y del Libertador General Bernardo O'Higgins. Servicio Nacional de Geología y Minería, Mapas Geológicos 2: 20 p., 1 mapa 1:100.000. Santiago.

Wall, R.; Sellés, D.; Gana, P. 1999. Area Tiltil-Santiago, Región Metropolitana. Servicio Nacional de Geología y Minería, Mapas Geológicos 11, 1 mapa 1:100.000, 1 anexo. Santiago.

Wyss, A.R.; Flynn, J.J.; Norell, M.A.; Swisher, C.C.III.; Novacek, M.J.; McKenna, M.C.; Charrier, R. 1994. Paleogene mammals from the Andes of Central Chile: a preliminary taxonomic, biostratigraphic, and geochronologic assessment. American Museum Novitates, No. 3098: 1-31.

Yáñez, G.; Rivera, O. 2009. Geophysical constraints of the Mapocho El Volcán (MEV-B) , and Its Geological Significance. *In* Congreso Geológico Chileno, No. 13. Actas S09-094: 4p. Santiago.

Yáñez, G.A.; Gana, P.; Fernández, R. 1998. Origen y significado geológico de la Anomalía Melipilla, Chile central. Revista Geológica de Chile 25 (2): 175-198. doi: 10.5027/andgeoV25n2-a05.

Yáñez, G.; Cembrano, J.; Pardo, M.; Romero, C.; Sellés, D. 2002. The Challenger-Juan Fernández-Maipo major tectonic transition of the Nazca-Andean subduction system at 33-34°S: geodynamic evidence and implications. Journal of South American Earth Sciences 15 (1): 23-38.

Yáñez, G.; Rivera, O.; Comte, D.; Pardo, M.; Baeza, L.; Vera, E. 2008. Damage zone and the occurrence of world-class porphyry copper deposits in the active margin of Chile: Geophysical signatures and tectonomagmatic inferences. *In* International Symposium on Andean Geodynamics, No. 7: 592-593. Nice.

Manuscript received: July 29, 2014; revised/accepted: April 2, 2015; available online: April 2, 2015.